Glassy dynamics in active epithelia emerge from an interplay of mechanochemical feedback and crowding.

Sindhu Muthukrishnan[1], Phanindra Dewan[2], Tanishq Tejaswi[1], Michelle B Sebastian[1], Tanya Chhabra[1], Soumyadeep Mondal[2], Soumitra Kolya[3], Sumantra Sarkar[2]*, Medhavi Vishwakarma[1]*

1. Department of Bioengineering, Indian Institute of Science, Bangalore, India
2. Department of Physics, Indian Institute of Science, Bangalore, India
3. Tata Institute of Fundamental Research, Hyderabad, India

Correspondence: medhavi@iisc.ac.in and sumantra@iisc.ac.in

Abstract

Glassy dynamics in active biological cells remain a subject of debate, as cellular activity rarely slows enough for true glassy features to emerge. In this study, we address this paradox of glassy dynamics in epithelial cells by integrating experimental observations with an active vertex model. We demonstrate that while crowding is essential, it is not sufficient for glassy dynamics to emerge. A mechanochemical feedback loop (MCFL), mediated by cell shape changes through the contractile actomyosin network, is also required to drive glass transition in dense epithelial tissues, as revealed via a crosstalk between actin-based cell clustering and dynamic heterogeneity in experiments. Incorporating MCFL into the vertex model reveals that glassy dynamics can emerge even at high cellular activity if the strength of the MCFL remains high. We show that the MCFL can counteract cell division-induced fluidisation and enable glassy dynamics to emerge through active cell-to-cell communication. Furthermore, our analysis reveals the existence of novel collective mechanochemical oscillations that arise from the crosstalk of two MCFLs. Together, we demonstrate that an interplay between crowding and active mechanochemical feedback enables the emergence of glass-like traits and collective biochemical oscillations in epithelial tissues with active cell-cell contacts.

1. Introduction

Glass transition is a kinetic phenomenon where a material falls out of equilibrium as its molecular motion slows down dramatically[1–3]. Similar behaviour is observed in crowded granular matter and in dense systems of self-propelled particles- when activity diminishes, particles jam with locally cooperative clusters, displaying typical traits of dynamic heterogeneity[4–6]. Interestingly, epithelial cells also show glassy traits when cell density rises to a homeostatic state. This has been observed in 2D cell monolayers[7–10], in organoid cultures mimicking organ architecture[11,12] and *in vivo*[13,14], suggesting cells tend to be at the brink of glass transition when they pack to form tissues[15,16]. However, unlike passive glass formers, living epithelial cells are inherently active due to the cycle of life and death, metabolic activity, and intercellular communication. Theoretical studies suggest that energy flux due to cellular activity should fluidise the system and prevent glass transition [17–20]. Indeed, mean-field models, e.g., the canonical vertex models, predict glassy behaviour only at diminished cell activity and high cell density[18,21,22]. However, such a frozen state in active biological cells is unrealistic; in fact, experimental analysis shows sub-Arrhenius relaxation dynamics of epithelial cells[7–9,23] , meaning the system remains more mobile than traditional glass

physics would predict at high densities[23,24]. The presence of dynamic heterogeneity in active epithelial monolayers suggests that crowding alone may not be sufficient to explain the glassy features in epithelial tissues, and this missing link could explain the discrepancy between theoretical predictions and experimental observations. Hence, we identify two problems: first, if

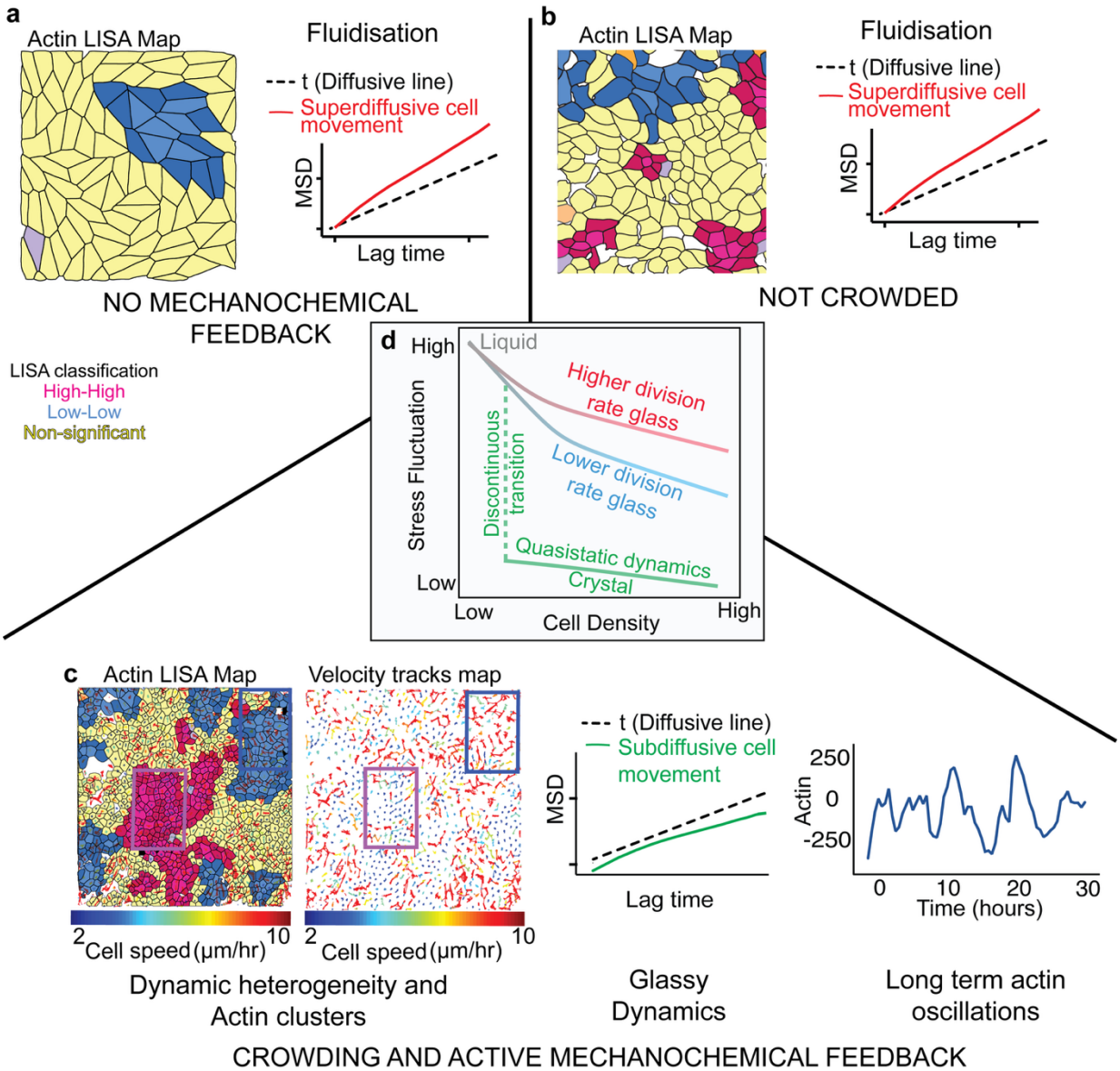

crowding alone is insufficient, what other factors drive the glass transition in epithelial tissues?

Figure 1: Crowding and Mechanochemical Feedback are necessary for the emergence of glassy dynamics, collective oscillations and spatial clustering of actin in epithelia: a) *In the absence of mechanochemical feedback, crowding of the tissue through cell division leads to fluidisation, as revealed by the Left-highly anisotropic shapes from the 1/Area LISA (Local Indicators of Spatial Association) map from our vertex model simulation, where 1/Area is proportional to Actin levels and the Right- superdiffusive mean squared displacement (MSD) of the cells from our vertex model and previous studies[17-22] . LISA clusters highlight groups of neighbouring cells with similar Actin levels (High-High: Pink and Low-Low: Blue), and cells that are not correlated with their neighbors are classified as Non-Significant (Yellow).* ***b)*** *Mechanochemical feedback without crowding does not lead to glassy dynamics: Right- the MSD remains superdiffusive, and Left- the cells do not form well-defined Actin clusters.* ***c)*** *Crowding and*

mechanochemical feedback together lead to glassy dynamics. We observe coexisting jammed and unjammed clusters of cells with different motilities, and the MSD becomes subdiffusive revealing dynamic heterogeneity and caging. Furthermore, the cells oscillate collectively with hour-scale time periods. ***d)*** *The observed glass transition is driven by cell density. Akin to temperature-driven passive glass transition, if the cell density is changed slowly, the tissue undergoes a discontinuous fluid-solid phase transition (green). However, if the density is increased sufficiently rapidly, such as through cell division, the tissue can avoid the discontinuous transition and undergo a glass transition (red and blue) at a density that depends on the division rate: a higher division rate leads to a faster glass transition (red).*

And second, how can we incorporate these factors in a model so that biologically correct features can emerge from simulations? We approached these questions by mapping cytoskeletal rearrangements that accompany cell crowding[25–28] to mechanochemical feedback loops. Mechano-transduction via the actin cytoskeleton allows cells to adapt to shape changes by modulating actin fibres and the contractile network. We anticipated that local clustering due to the presence of jammed and unjammed regions would be reflected in biochemical markers such as actin, and such bio-physical crosstalk will modulate global tissue dynamics. We used *LifeAct* MDCK epithelial cells and performed time-lapse imaging to map changes in the actin cytoskeleton as dynamic heterogeneity emerges. We found clear correspondence between actin expression and jammed and unjammed clusters, indicating that active mechanochemical feedback drives glass transition in epithelial cells. We incorporated the observed mechanochemical feedback in an active vertex model, which couples changes in cell area and cell perimeter to the underlying signalling of the contractile actomyosin network. Incorporating this feedback into the model allowed clusters of dynamic heterogeneity to emerge, even at high cell division rates, thereby engendering glassy dynamics in the presence of strong biological activity. Additionally, from experiments and the model, we report collective hour-scale actin oscillations in the cells, unlike the previously reported minute-scale oscillations. We explain the increased oscillation timescales via mechanochemical feedback, which stabilises emerging biophysical clusters. When feedback strength is lowered or cell density is decreased, the collective oscillation disappears, and cells oscillate with minute-scale time periods, similar to the oscillations observed in isolated cells. We show that the oscillations originate from the crosstalk between the mechanochemical feedback loop-I, which depends on load-dependent actomyosin binding, and another mechanochemical feedback loop-II, which couples the actin cytoskeleton to the biochemistry of the Hopf oscillator ERK. Together, we establish that active mechanochemical feedback enables the emergence of glassy dynamics through active cell-to-cell interactions and crowding.

2. Results:

2.1 Interplay of crowding and mechanochemical feedback dictates emergence of glassy dynamics

Considering that actin rearrangement is downstream of most mechanochemical changes in cells, we first investigated any possible coupling between glassy dynamics and actin expression in the epithelial monolayer at homeostasis (Fig. 2a). We compared velocity fields with spatial actin distribution patterns from time-lapse imaging data of MDCK cells tagged for Actin (Supplementary video 1 and Fig. 2b). Spatial organisation of F-actin was computed using local Moran's index, thus allowing us to generate Local Indicators of Spatial Association (LISA)[28] maps (Fig. 2a and 2c), which classified cells into clusters representing regions of spatially correlated F-actin levels. Velocity tracks (Fig. 2d) revealed coexisting slow and fast-moving clusters at a densely packed state (Fig. 2c, d), indicating dynamic heterogeneity, a hallmark of glassy systems. Additional features of glassy dynamics were also observed, including subdiffusive

mean squared displacement and caging (Fig. 2e), and a sub-exponential decay in the overlap function (Q(t), Fig. 2f). To capture the link between the dynamic clusters arising from glassy behaviour and the biochemical organisation of cells, we quantified the spatial organisation of F-actin using LISA and found 'High-High' & 'Low-Low' actin clusters, where neighbours correlated in actin expression. We termed those as hotspots and coldspots, respectively (Fig. 2c, Extended Data Fig. 1c). Interestingly, slow-moving, jammed regions aligned with actin hotspots, whereas fast-moving, unjammed regions corresponded to actin coldspots (Fig. 2c and 2g), indicating that glassy dynamics and actomyosin organisation are linked. From traction force microscopy experiments (Fig. 2h and 2i), we found that cellular tractions and actin expression are negatively correlated; specifically, unjammed coldspots displayed higher traction forces, whereas jammed hotspots displayed lower traction forces (Fig. 2j). While higher traction in unjammed cells is intuitive due to increased movement, the inverse correlation between actin clusters and both cellular movement and forces suggests that dynamic heterogeneity manifests itself in biochemical signatures through mechanochemical feedback and thus may directly affect tissue functionality by modulating cells' internal machinery. Since crowding is essential for dynamic heterogeneity to emerge in active and passive glass formers, we wondered whether biochemical clustering is also modulated at different levels of crowding.

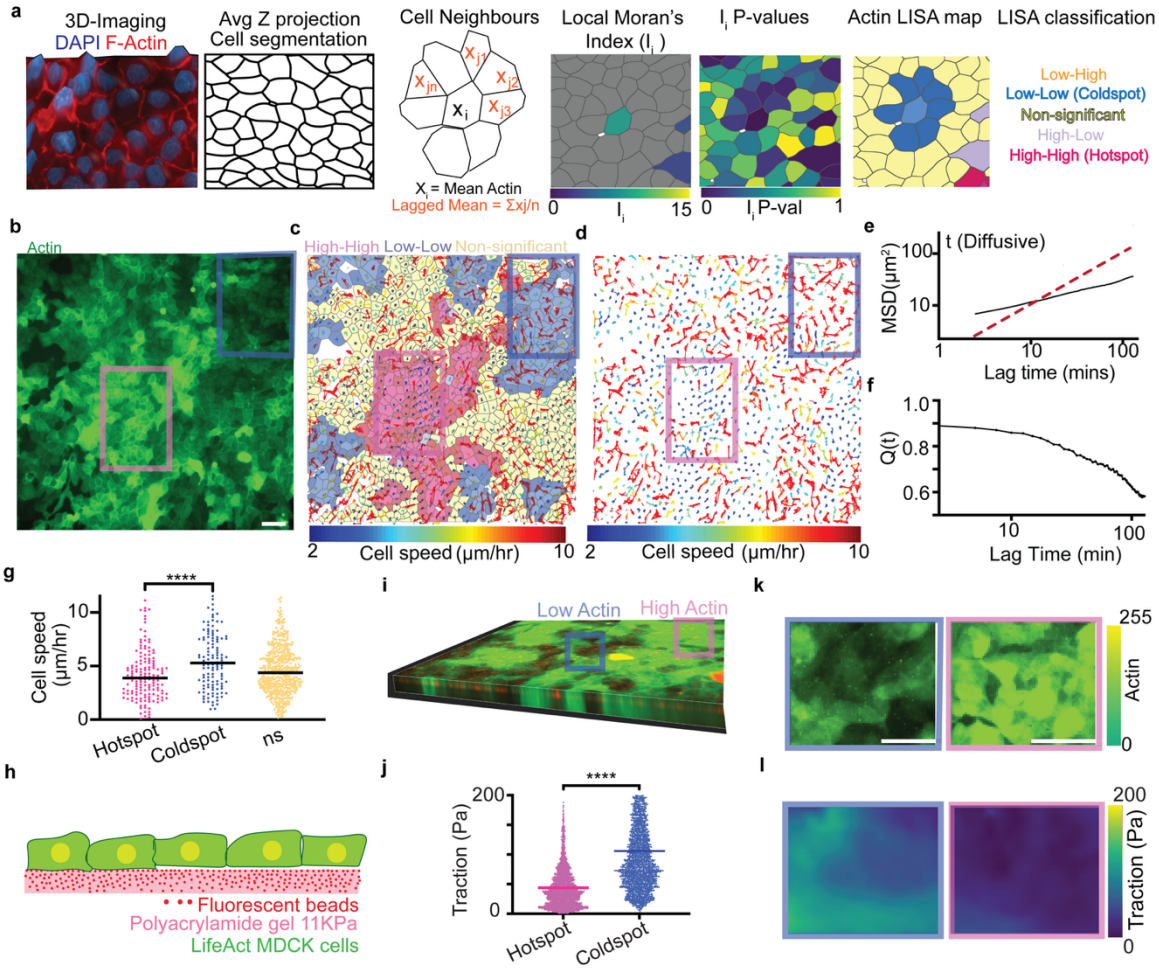

Fig 2: Spatial distribution of Actin and forces follows the dynamic heterogeneity landscape: *a)Schematic of Moran analysis with segmentation andcustom R code, b) Representative image from timelapse microscopy of LifeAct-MDCK cells, c) Cell tracks overlaid on F-Actin LISA map, d) Cell trajectories obtained from tracked cells, e) Mean Square*

*Displacement (MSD) plot for one representative timelapse movie of cells, f) Self-overlap function (Q(t)) plot for one representative timelapse movie of cells, g) Actin levels in groups of fast and slow cells and in non-correlated velocity regions, h) Schematic of traction force microscopy, i) Image of cells (green for Actin) and fluorescent beads (red), j) Traction magnitude at Actin hotspots and coldspots, k) Left- Traction heatmap (top) at low Actin (bottom) regions and right- Traction heatmap (top) at high Actin regions (bottom). Unpaired t-test: *p < 0.05, **p < 0.01, ***p < 0.001, ****p < 0.0001. Scale bars= 50µm. Lines represent the median.*

Indeed, LISA maps of F-actin in low- and high-density monolayers (Fig. 3a and 3b) showed differences in locally correlated clusters: loosely packed monolayers had smaller clusters, and densely packed monolayers had larger clusters (Fig. 3c). Global Moran's index, a metric for spatial correlation in actin among neighbours, increased for densely packed monolayers (Fig. 3d). Furthermore, in loosely packed monolayers, the mean squared displacement was not subdiffusive (Fig. 3e) and the decay in the overlap function was faster than in a densely packed monolayer (Fig. 3f), suggesting that crowding is essential for the emergence of glassy dynamics. PIV analysis also showed subdiffusive dynamics in a densely packed monolayer, but diffusive dynamics in a loosely packed monolayer (Extended Data Fig. 2k-m.). We also observed global differences in cell adhesions and contractility, as indicated by the overall lower intensity of actin in low-density monolayers, but longer and more numerous actin stress fibres compared to high-density monolayers (Extended Data Fig. 2a-d). In densely packed monolayers, cortical actin was higher, stress fibres were shorter and less numerous, and overall actin intensity was higher (Extended Data Fig. 2a, b). Additionally, myosin and E-cadherin also showed higher expression and cortical localisation in densely packed monolayers (Extended Data Fig. 2a, b). These results indicate an active interplay between crowding and mechanochemical feedback in dictating cell clustering and glassy behaviour at homeostasis.

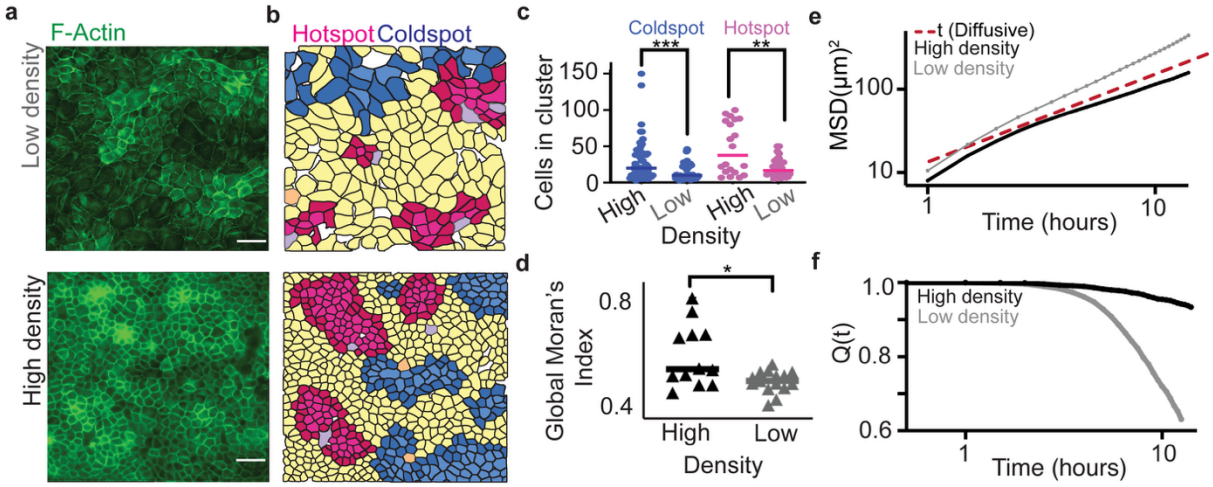

Fig 3: Higher spatial clustering with increasing density: *a) Immunocytochemistry of Actin at low (top) and high (bottom) density, b) LISA cluster maps of Actin at low (top) and high (bottom) density, c) Number of cells in hotspots and coldspots at high and low density, d) Global Moran's Index at low and high density, e) Mean Square Displacement (MSD) plots for low density (Gray) and ligh density (black) monolayers, f) Self Overlap function Q(t) plots for low density (Gray) and high density (black) monolayers. Scale bars=50µm. *p=0.017. Here, low and high density monolayers refer to loosely and densely packed monolayers, respectively. Scale bars= 50µm. Lines represent the median.*

2.2 An active vertex model with mechanochemical feedback and crowding undergoes a glass transition

To delineate the role of crowding and mechanochemical feedback individually, we developed an active vertex model with dynamic cell shapes, where cell division and mechanochemical feedback loops (MCFLs) were integrated and tuned. To this end, we considered the crosstalk of two MCFLs. The MCFL-I arises from load-dependent binding of myosin to actin[29–31] (Fig. 4a). In the model, its effect is captured by cell area (A) dependent variation of the vertex model parameters A_0 and P_0 (SI-theory). Since actin intensity is inversely proportional to the cell area (SI-theory), we assume a constant total cellular F-actin. Moreover, as the tissue matures, F-actin and myosin localise near the cell-cell junctions at the expense of the stress fibres (Fig. 4a and Extended Data Fig. 2a), suggesting an increase in line tension, but reduced contractility as the cell area decreases upon crowding. Because contractility is equal to $(\Gamma/K)A_0^{-1}$ and tension to $-(\Gamma/K)(P_0/A_0^{3/2})$ [32,33], compression due to cell crowding decreases P_0 and increases A_0-captured by two coupled positive (IA) and negative (IB) loops, respectively, which we collectively term MCFL-I. Here, Γ and K are the perimeter and area elasticity coefficients, respectively, of the vertex model (SI-theory). The second mechanochemical feedback loop, MCFL-II, arises from the feedback between ERK (extracellular signal-regulated kinase) and actin cytoskeleton[34–36] (Fig. 4a). ERK signalling is tightly linked to the regulation of the actin cytoskeleton via modulating phosphorylation of numerous actin-regulatory proteins[37–42]. ERK acts as a Hopf oscillator[43], allowing for actin and other biochemical oscillations in mammalian cells, which enables cells to translate external signals into rhythmic intracellular behaviours[44–47]. Because the two MCFLs share common elements, we expect collective behaviours to emerge from extensive crosstalk between them, as seen from the equations governing the MCFLs, shown below (the subscripts I and II show the origin of the terms).

$$
\begin{aligned}
\partial_t M &= a - (b+1)M + cM^2E \\
\partial_t E &= bM - cM^2E - DE \\
\tau_D \partial_t D &= -(D - D_0) - [\,\beta D(A-1)\,]_{\mathrm{II}} \\
\tau_A \partial_t A_0 &= -\left[\,A_0 - \hat{A}_0(A)\,\right]_I - [\,\alpha(E - E_0)\,]_{\mathrm{II}} \\
\tau_P \partial_t P_0 &= -\left[\,P_0 - \hat{P}_0(A)\,\right]_I - \left[\,\alpha(E - E_0)/\sqrt{A_0}\,\right]_{\mathrm{II}}
\end{aligned}
$$

Here, M, E, D model a simplified chemistry of the Hopf oscillator ERK[36], denoted by E. M is an activator of E, whereas D is a degrader of E. In the absence of MCFL-II, A_0 and P_0 relax to $\hat{A}_0 = 2a_0 p_{bound}$ and $\hat{P}_0 = 2\hat{q}_0\sqrt{a_0}(1 - p_{bound})$, where $p_{bound} = 1/[1 + (A/\hat{A})^2]$ is the fraction of myosin bound to F-actin (SI-theory), $a_0 = 1$ is the A_0 if $A = \hat{A}$, and $\hat{q}_0$ is the shape index for the same condition. $\hat{A}$ measures the strength of MCFL-I and is inversely proportional to the binding affinity of myosin binding to actin (SI-theory). $\mu = \alpha\beta$ measures the strength of MCFL-II[34–36]. Here, we vary $\hat{A}$, keeping μ fixed, to explore the role of cell division and mechanochemical feedback on glassy tissue dynamics.

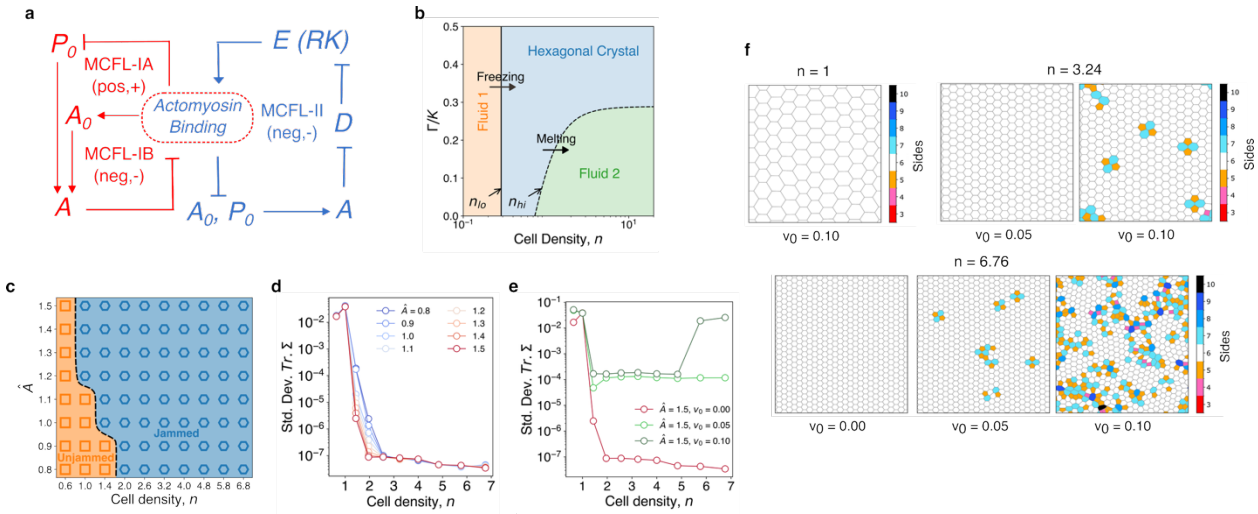

Figure 4 ***Ground states of active vertex model with cell division and mechanochemical feedback:*** *(a) A schematic showing the crosstalk of MCFL-I and MCFL-II. (b) Ground state phase diagram of the vertex model with only MCFL-I shows two discontinuous transitions. The first is from a fluid (Fluid-1, orange) to a crystal (blue) phase at density n_{lo} (solid black line) and the second is from a crystal to a different fluid (Fluid-2, green) at n_{hi} (dashed black line). (c) A phase diagram of the model from constant density (n) simulations in the absence of motility(v_0), showing the transition from unjammed (shape index > 3.81) to jammed (shape index ≤ 3.81) states. The transition is qualitatively similar to the transition from the Fluid-1 to the crystalline state (Summary figure) (d) Stress fluctuation as a function of cell density for different $\hat{A}$ shows the discontinuous phase transition from the fluid-1 to the crystalline state in the absence of motility. (e) The discontinuous transition from the Fluid-1 to the crystalline state remains in the presence of motility. However, at high enough motility, the crystal undergoes defect-driven discontinuous 2D-melting to Fluid-2 phase. (f) Configurations at different densities and motilities exhibit distinct phases: Fluid-1 ($n = 1$), Crystalline ($n = 3.24, v_0 = 0.05$ and $n = 6.76, v_0 = 0{,}0.05$), and Fluid-2 ($n = 6.76, v_0 = 0.1$).*

To determine whether this model exhibits a glass transition driven by cell division, we first analysed the ground state properties of the vertex model in the absence of MCFL-II and motility, but in the presence of MCFL-I. Because MCFL-I couples cell density to tissue mechanics, our ground state analysis establishes key phase transitions driven by cell density n. Incorporating motility and MCFL-II just moves the boundary of the transitions. The ground state behaviour of the model depends on the parameters Γ/K, $\hat{q}_0$ and $\hat{A}$. In particular, a crystalline ground state, characterised by a nonzero shear modulus, $\bar{G}$, appears discontinuously at a density n_{lo} that does not depend on Γ/K, but increases with increasing $\hat{q}_0$ and decreasing $\hat{A}$ (SI-theory). This is the well-known rigidity transition in the canonical vertex model[32,48], driven here by cell density (Fig. 4b). Surprisingly, for $\Gamma/K < 1/2\sqrt{3} \approx 0.29$, another discontinuous transition occurs at a high density n_{hi}, where the monodisperse crystalline state transitions to a polydisperse fluid phase (Fig. 4b). n_{hi} diverges as $\left(1/2\sqrt{3} - \Gamma/K\right)^{-1/2}$. Hence, in the ground state, the high-density phase transition disappears for $\Gamma/K > 1/2\sqrt{3}$ (Fig. 4b, SI-theory), implying that for MDCK tissues, for which $\Gamma/K \approx 0.32$[30], this melting transition would not exist in the ground state.

Next, we explored whether these transitions persist during simulations, which occur away from the ground states due to topological transitions, motility, and other active forces. To characterise the behaviour of the model at different cell densities n and feedback strengths $\hat{A}$, we first performed constant density simulations, allowing the model to find energy-minimised states. First, we used the standard criterion, the mean shape parameter $\langle q \rangle \approx 3.81$ at the jamming transition, to construct a phase diagram (Fig. 4c). This showed that the density at which the jamming transition

occurs decreases with $\hat{A}$, similar to n_{lo}. Next, we used stress fluctuation (standard deviation of the trace of the force-moment tensor, Σ) as a metric to probe this rigidity transition: low and high fluctuations correspond to solid and fluid states, respectively (SI-theory). In the absence of motility, the constant-density simulations show only a single discontinuous transition at n_{lo}, consistent with the ground state analysis (Fig. 4d). Adding motility introduces the second fluidisation transition at densely packed monolayers through defect-driven 2D melting (Fig. 4e-f, akin to the behaviour at n_{hi}. Above n_{lo}, stress fluctuation changes discontinuously to a value that is many orders of magnitude lower than value just below n_{lo}[1,3,23]. Hence, we expect that if the density is increased sufficiently rapidly, such as through cell division, the tissue will avoid crystallisation and transition to a glassy state.

This is indeed what we observe. Increasing density through constant division rate simulations at different division rates r, we find that at sufficiently low densities, irrespective of the division rates, the stress fluctuations decay at the same rate as the fluid state in the quasistatic simulations (Fig. 5a, Extended Data Fig. 4c), indicating that a unique fluid state exists at these densities. As the density is increased, the system falls out of the fluid phase at a density that depends on the division rate. The higher the division rate, the more rapidly the system falls out of the fluid phase, and the stress fluctuation starts decaying at a slower rate. This observation parallels the phenomenology of passive glass transition, where similar cooling rate dependence is also observed[1,3]. Hence, we claim that at constant division rates, the tissue undergoes a glass transition (Fig. 5a, Extended Fig. 4c).

Because tissue rigidity transition is driven by changes in cellular shapes[25,49], we tested whether the glass transition is also manifested in the parameters describing the cell shapes. To do so, we computed the anisotropy of the cell shape through the mean asphericity (SI-theory), κ, as a function of n. In the quasistatic limit ($r = 0$), κ decreases monotonically in the absence of motility, but shows a nonmonotonic increase in the presence of motility (Fig. 5b, Extended Data Fig. 4a,b). In particular, in the presence of motility κ is minimum, i.e. the cells are most isotropic, just above n_{lo}. However, whereas κ increase is dependent on $\hat{A}$ for $n < n_{lo}$, it is independent of $\hat{A}$ when $n > n_{lo}$, suggesting that while $\hat{A}$ governs the mechanics of the fluid phase, the mechanics of the crystalline phase is governed only by the cellular density n in the quasistatic limit (Extended Data Fig. 4b). For simulations with nonzero division rates and motility, the κ trajectory deviates significantly from the quasistatic limit (Fig. 5b, Extended Data Fig. 4d). The rate-dependence of the glass transition is observed here as well; systems with lower division rates show a lower κ in the glassy phase. To experimentally verify these results, we perturbed the tissue with Blebbistatin (Extended Data Fig. 5), which simultaneously lowered r and $\hat{A}$. By segmenting the cells, we computed κ at different densities n under various treatment conditions (Fig. 5c). Consistent with our theoretical observations, we find that the lower division rates at higher Blebbistatin concentrations led to a delayed transition, as indicated by lower κ values at the same densities at higher Blebbistatin concentrations (Fig. 5c). Furthermore, as observed in the simulations (SI-theory), these differences disappear at higher densities, which further corroborates our claim.
prove beyond doubt that the observed dynamics arises from an underlying glass transition, we next computed the MSD (Fig. 5d) and the overlap function ($Q(t)$, Fig. 5e), both of which showed

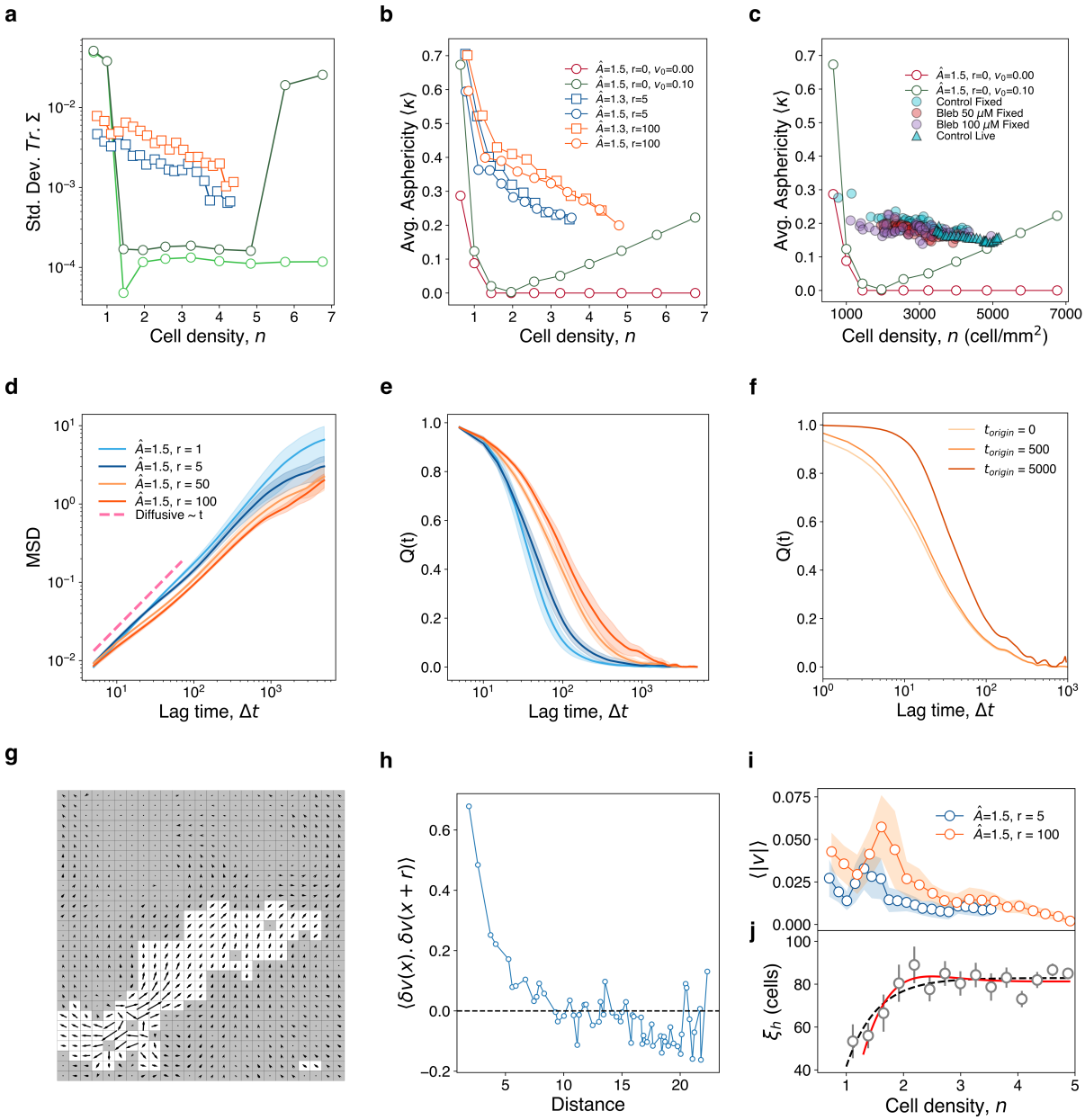

Figure 5 ***Glassy dynamics in the vertex model:*** *(a) Stress fluctuation decay with density depends on the rate of cell division, akin to the cooling rate dependence of passive glass transition. The discontinuous constant-density simulation data are also shown for reference (see legends in b). (b) Mean asphericity of the cells, κ, shows a similar rate dependence. In the absence of motility, κ decays discontinuously with n. (c) Mean asphericity of untreated and Blebbistatin-treated cells shows trends similar to simulations performed at different division rates, which is consistent with the known effect of Blebbistatin on epithelial cells. We have assumed* $n = 1$ *to correspond to 1000 cells/mm*^{2}*. (d) Mean squared displacement as a function of lag time for different division rates shows faster transition to subdiffusive plateaus at higher division rates. (e) The overlap function Q(t) exhibits similar behaviour, suggesting that the tissue transitions into the glassy state more rapidly at a higher division rate (see legends in d). The shaded regions indicate the standard deviation. (f) Q(t) calculated with respect to different time origins (for trajectories of the cells in simulation) shows ageing. (g) The simulations show persistent dynamic heterogeneities and (h) the spatial correlation of velocity has a nonzero correlation length. Consistent with prior experiments, (i) the cell motility decreases steadily with density and (j)* ξ_h*, the size of dynamic heterogeneity increases with cell density. The markers show mean* ξ_h*. The black dashed line shows a best fit line, and the red solid line shows a fit with overshoot. For all the panels (except h), we simulated a system with 10x10 box size, corresponding to 100 cells at* $n = 1$*. Panel h is calculated from a simulation of a system with 40x40 box size. For all panels, error bars or shaded regions indicate standard deviation.*

Flattening at intermediate timescales at all r. In particular, the relaxation of $Q(t)$ shows the classic signatures of ageing (Fig. 5f). Additionally, the flattening was more pronounced at higher division rates, which is consistent with our claim that the glass transition occurs sooner for higher division rates. Although this observation contradicts previous theories describing glassy dynamics in biological cells, where a high division rate enhances fluidisation[17,21,22,50], it agrees with experiments describing glassy dynamics in epithelial cells[7–10,13,14,25,51–55]. Next, we calculated the cell velocities from the simulations, which exhibited features of dynamic heterogeneity (Fig. 5g) and nontrivial spatial correlations (Fig. 5h). Additionally, the mean speed of the cells decreased rapidly with increasing density (Fig. 5i), while the size of the dynamic heterogeneity, ξ_h, increased (Fig. 5j). These observations are consistent with prior experiments on glassy tissue dynamics[7,8,10], which establishes our claim.

2.3 Mechanochemical feedback stabilises activity clusters to generate long-term collective oscillations

The glass transition, driven by crowding and mechanochemical feedback, enables cells to assemble into jammed and unjammed clusters, characterised by high and low actin levels, respectively. Next, we wondered about the stability of these clusters over time and whether collective temporal patterns in biochemical signalling can emerge as a result of dynamic heterogeneity. We performed time-lapse imaging of *LifeAct* MDCK cells and measured actin Because the dynamics of actin at hotspots and coldspots are different, we reasoned that dominant time-periods might result from these distinct clusters of cells. Indeed, hotspots exhibited dominant 11-hour oscillations while coldspots showed 4-hour oscillations (Fig. 6c, d, f). Similar oscillatory behaviour was also observed in traction force analysis, which showed global oscillations over a timescale of several hours (Supplementary Fig. 3). These results indicate that dynamic heterogeneity clusters are also synchronised in their biochemistry, with correlated and stabilised actin expression that oscillates over a timescale of several hours.

Here, unjammed clusters were found to be more dynamic than jammed clusters, as reflected in locally distinct oscillation timescales. Furthermore, the oscillation amplitude decreased as cell density rose over time, as captured through the decay of wavelet power over time (Fig 6e and Extended Data Fig. 3i), while the dominant time period increased (Fig. 6e and Extended Data Fig. 3h, i). Interestingly, oscillations in ERK and actin signal are reported in mammalian cells before, including in immune cells[56], and in embryonic stem cells[57,58]. However, in those studies, oscillations are over timescales of several minutes. Interestingly, *lifeAct* MDCK cells, when cultured as single cells, i.e. in the absence of cell-cell interactions, show oscillatory behaviour of actin with a period of approximately 20 mins (Fig. 6a). The transition from minutes timescale of actin oscillations in single cells, to hours timescale of oscillations in crowded monolayer reflects the coupling of glassy dynamics to cellular biochemistry, allowing for stabilised biochemical signalling in the local dynamic heterogeneity clusters.

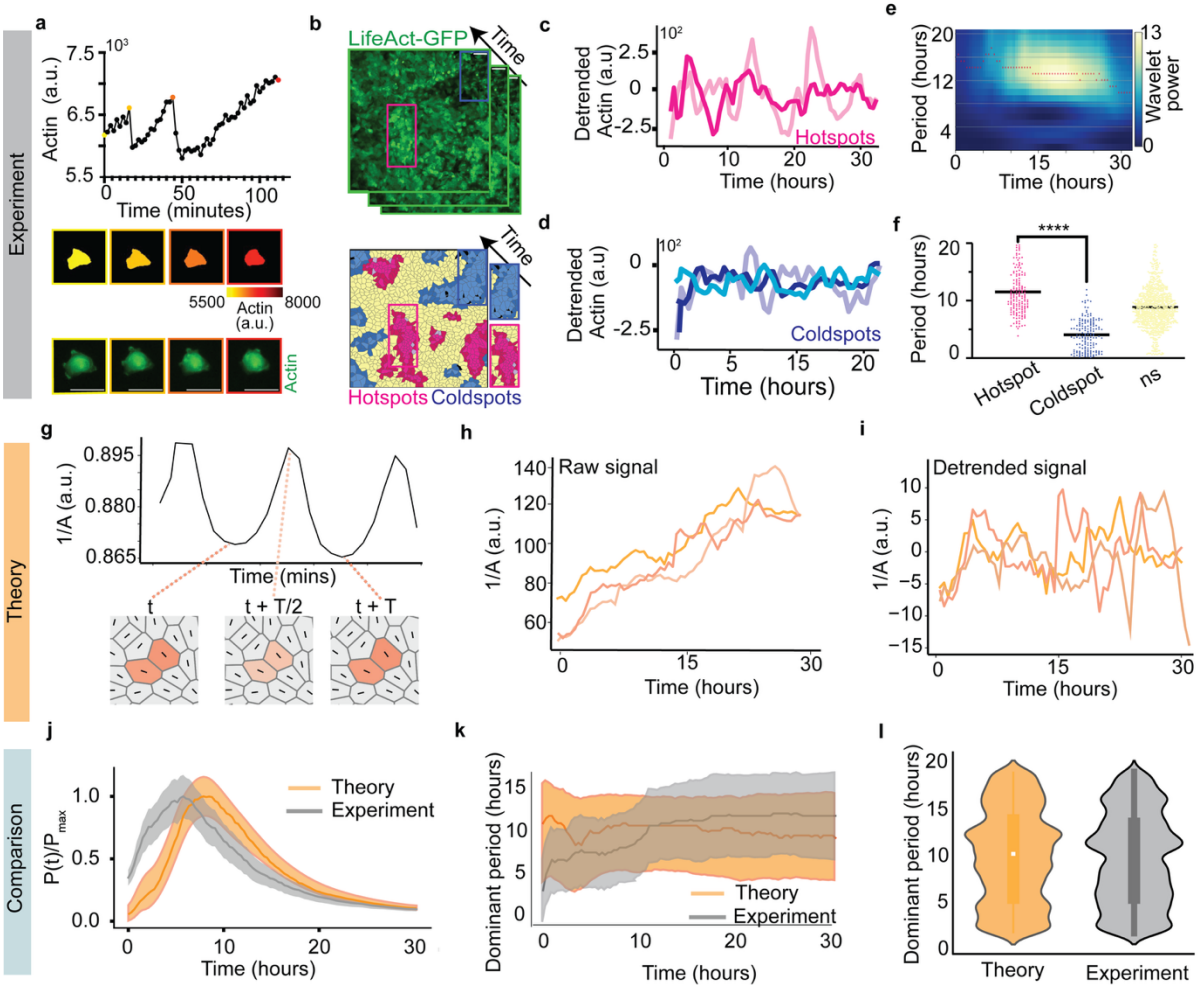

Figure 6 ***Spatially collective temporal dynamics from the crosstalk of MCFL-I and MCFL-II:*** *a) Single MDCK cells show periodic actin oscillations of ~ 20 min period. Top- Plot showing Actin intensity over time in single MDCK cells without neighbours. Raw images of single cells (bottom), and cell images pseudocolored for Actin (middle). The color of the box around the images (middle and bottom) correspond to the timepoint of the image corresponding to the coloured dots in the top image. b) In contrast, confluent epithelia (top) exhibit collective temporal actin oscillations that depend on spatial actin distribution (bottom), c) Actin hotspots show oscillations with ~10-hour period, d) and Actin coldspots show faster oscillations with ~4-hour period. e) Wavelet analysis of the detrended experimental signals shows decreasing wavelet power and increasing period over time, f) Comparison of dominant period at the hotspots and coldspots, g) Our model predicts single cell area oscillation of $T \sim 18$ min period, originating from the MCFL-II. h) Because the actin level in the cell is proportional to $1/A(1/A)$, the latter is plotted here as a function of time, i) Detrended $1/A$is plotted as a function of time, j) Distributions of oscillation power over time, and k) Distributions of oscillation period over time show quantitative match between theory and experiments, l) Comparison of the dominant oscillation period from theory and experiment. Scale bars=50μm. Lines represent the median.*

To probe this hypothesis, we explored the role of MCFL-II in regulating tissue dynamics. In the model, the negative feedback loop in MCFL-II couples the nonlinear chemistry of ERK with the mechanics of the actin cytoskeleton (Fig. 4a). It has been shown earlier that MCFL-II, by itself, generates collective oscillations and travelling waves in the absence of cell division[34–36]. In contrast, here, it is coupled to the glassy dynamics induced by cell division and MCFL-I, which should change the nature of the oscillations. Owing to the inverse relationship between actin and cell area in the experiments (SI-theory), we plotted $1/A$ over time to predict cellular actin dynamics. Our model predicts high-frequency cellular actin oscillations, with a period of approximately 18 minutes, for loosely packed monolayers (Fig. 6g), similar to the single-cell

oscillations observed in our experiments (Fig. 6a). However, it exhibits a non-oscillating state for densely packed monolayers, punctuated by collective oscillations with a period of several hours at intermediate densities, owing to mechanochemical feedback originating from cell-cell contacts (Fig. 6h-i). Using our model, we can explain the mechanism underlying the collective oscillation as follows. Cell division generates daughter cells with small areas that are stabilised by MCFL-I in the jammed regions. As cell area decreases over time, ERK and actin undergo compression-induced oscillation death[36], causing MCFL-II oscillations to dampen. This manifests as a progressive loss of oscillation amplitude over time (Fig. 6j), increased median oscillation periods (Fig. 6k), and broadly distributed time periods (Fig. 6l), consistent across experiments and the model.

Together, we show that in epithelia, biochemical and mechanical signalling modulate each other via mechanochemical feedback loops, resulting in glassy dynamics and unique spatiotemporal oscillations.

3. Discussion

Epithelial homeostasis, essential for organ function, relies on regulating cell density and shape. Experiments and theory reveal spatial variability in cell shapes, driven by cell activity, communication, and deformability. Notably, temporal analysis of crowded epithelial cells reveal glassy dynamics with typical features including caging, local cooperativity and subdiffusive movement. In contrast to these experimental observations, theoretical studies suggest that cellular activity should fluidise the system and prevent the glass transition [17–20]. Indeed, mean-field models, e.g., the canonical vertex models, predict that glassy features can only occur when cell activity is minimal and cell density is very high[18,21,22] -- a frozen state that is unrealistic for epithelial cells, which, in reality, exhibit sub-Arrhenius relaxation dynamics[7–9,23] upon crowding. Due to this mismatch between theoretical predictions and experimental observations, the emergence of glassy dynamics in epithelial cells remains elusive. We identified a missing link in the traditional, crowding-based explanation for glassy dynamics in epithelial tissues, and suggest that cell-to-cell communication may dictate emergent cellular dynamics. Furthermore, the canonical vertex model is insufficient to capture these emergent dynamic heterogeneities in epithelial cells, largely due to its inability to account for dynamic shape changes. Here, we experimentally demonstrate that dynamic heterogeneity clusters are associated with biochemical clustering, and that this association is dictated by an interplay between mechanochemical feedback and cell crowding. To delineate the roles of mechanochemical feedback and cell crowding, we developed an active vertex model with dynamic cell shapes, where cell divisions and mechanochemical feedback loops were integrated and tuned. Mechanochemical feedback loops result not only in glassy spatiotemporal relaxation but also in unique collective biophysical oscillations as observed in cellular actin levels, area, and traction forces. We observed two interesting trends: first, time period of emergent actin oscillations is several hours, as opposed to typical minutes time scale oscillations observed previously in mammalian cells, and second, time period of oscillations are distinct for locally jammed and unjammed clusters, with the less dynamic jammed clusters oscillating over 10 hours period, and the more dynamic unjammed clusters oscillating over 4 hours period, similar to the period of cell area oscillations in MDCK monolayers reported earlier[59]. Clustering of cells and

temporal oscillations are both perturbed if mechanochemical feedback is inhibited in the jammed state.

We also theoretically established that the epithelial glass transition is driven by cell density. By analysing the ground state of a vertex model with mechanochemical feedback, we show that a freezing transition occurs at a density that decreases with increasing feedback strength. Cell division enables the exploration of this parameter space by increasing cell density at a finite rate, which, if sufficiently rapid, leads to a glass transition. Together, we establish that an interplay between active mechanochemical feedback and cell density enables the emergence and stabilization of glassy dynamics in active epithelial tissues. The glass transition in biological cells has implications ranging from development of organs to diseases, and we are only now beginning to understand the biophysical crosstalk that leads to the emergence of such traits. While questions pertaining to the implications and relevance of glassy features in biological tissues still remain unanswered, we believe our study represents a first step towards enhancing the understanding of the spatiotemporal dynamics of epithelial cells, specifically revealing the emergence and maintenance of dynamic heterogeneity clusters through active cell-to-cell communication.

Methods

Cell culture:

Madin-Darby canine kidney cells MDCK cells, LifeAct-GFP MDCK cells were cultured in Dulbecco's Modified Eagle Medium (DMEM, Gibco) supplemented with 10 μmg ml^{-1} streptomycin (Pen Strep, Invitrogen), and 5% fetal bovine serum (FBS, Invitrogen) in a humidifier incubator maintained at 37°C and 5% CO_2.

Widefield Microscopy: Fluorescence imaging was carried out on a Zeiss Axio Observer 7 inverted microscope equipped with a scientific sCMOS camera (Iberoptics). Images were captured using both a 20× objective (air) or 40× objective (air) for live imaging and a 63× oil-immersion objective for immunofluorescence images that were used for LISA cluster analysis. For live experiments, the samples were placed in a stage-top humidified incubator and maintained at 37 °C with 5% CO_2 during the imaging.

Traction force microscopy:

Glutaraldehyde-activated glass-bottom dishes were used to cast thin polyacrylamide (PAA) gel substrates containing 0.5 μm fluorescent carboxylated polystyrene beads, as described previously[60]. These gel surfaces were then functionalized with sulphosuccinimidyl-6-(4′-azido-2′-nitrophenylamino) hexanoate (Sulfo-SANPAH, Thermo Scientific) and covalently coated with 0.5 mg ml^{-1} Fibronectin (Sigma) to ensure cell attachment. Cells are then seeded on the gels and grown until a confluent monolayer is obtained and imaged with the beads. Then, to get reference images, cells were trypsinised and resulting bead positions in relaxed state were obtained. Images were aligned to correct stage drift, followed by obtaining bead displacement vectors. From these vectors, traction stresses were reconstructed using regularized Fourier Transform Traction Cytometry[61] using the FTTC FIJI plugin.

Immunostaining:

457 Cell fixation was done with 4% formaldehyde diluted in 1× phosphate-buffered saline (PBS; pH
458 7.4) at room temperature (RT) for 10 min, followed by 1× PBS washes (three times). Cell
459 permeabilization was carried out with 0.25% (v/v) Triton X-100 (Sigma) in PBS for 10 min at RT,
460 followed by washing three times with PBS to remove the reagent. To block non-specific antibody
461 binding, samples were incubated in 2% BSA and 5% FBS in PBS at RT for 45 min. The blocking
462 buffer was removed after 45 min, and the primary antibody dilution (1:300) prepared in the
463 blocking buffer was added to the samples. The samples were incubated with the primary antibody,
464 at 4°C overnight. Then, samples were washed three times with 1× PBS. Each wash was done for
465 5 minutes on a gel rocker. Next, secondary antibodies tagged with a fluorophore were (1:300)
466 prepared in 25% blocking buffer diluted in PBS and added to the sample for 60 min at RT. To
467 counterstain cell nuclei, the samples were added with a DNA-binding dye, 4′,6-diamidino-2-
468 phenylindole (DAPI; 1 µg/mL in PBS, Invitrogen), along with the secondary antibody solution.
469 Then, thorough washing of the samples was done with PBS before imaging.
470 The following primary antibodies were used: Zo1- (1:200) (CST #5406), E-Cadherin (24E10) -
471 (1:500) (CST #3195), P-myosin (Ser19) (1:50) (CST #3671), Beta catenin (1:500) (CST #9562).
472 The following secondary antibodies were used: Alexa Fluor 488-conjugated anti-rabbit IgG
473 (1:500) (CST #4412), Alexa Fluor 488-conjugated anti-mouse IgG (1:500) (Invitrogen
474 #A32723), Alexa Fluor 594-conjugated anti-rabbit IgG (1:500) (CST #8889). F-Actin was statined
475 with Alexa Fluor 594-conjugated phalloidin (1:1000) (CST #12877S) and 4′,6-diamidino-2-
476 phenylindole (DAPI) (1:1000 and 1:2000) (CST #4083S) was used to stain the nucleus.
477
478 **Drug treatments:**
479 **Blebbistatin:**
480 For immunocytochemistry experiments, Blebbistatin (Sigma) was added at a final concentration
481 of 50µM and100µM after the monolayer reached high density, and dishes were fixed 6 hours after
482 the addition of the drug.
483
484 **Thymidine double block:**
485 Cells were treated with 2mM Thymidine (Sigma) and incubated for 16 hours. After this, they were
486 washed and cultured in regular cell culture media for 9 hours. Then, 2mM Thymidine was added
487 again and incubated for 14 hours. Cells were then washed and used immediately for experiments.
488
489 **<u>Image analysis</u>**
490 **Cell segmentation:**
491 Images were segmented with cellpose[62] to get the cell masks with Actin as the primary and DAPI
492 as the second channel in immuostained images. For segmentation in timelapse microscopy images,
493 phase-contrast images were used and were segmented with a custom trained model on cellpose.
494 Area, Perimeter, ellipse fit, and mean fluorescence intensity within masks were computed using
495 LabelsToRois plugin[63] in FIJI for fixed images and using Trackmate plugin for live microscopy
496 data. To remove wrongly segmented spots misidentified as cells by the software, cells were filtered
497 out based on area cutoff in subsequent analysis.
498
499 **Cell tracking:**
500 Cells were tracked using Trackmate[64,65] Plugin from the segmented images of Cellpose using the
501 Intersection of Union (IoU) method. Prior to tracking,wrongly segmented labels were removed
502 using the area filter on trackmate.
503

Moran's Index:

The Global Moran's Index[66] was calculated using the following definition:

$$I = \frac{n}{\sum_{i=1}^{n}\sum_{j=1}^{n} w_{ij}} \frac{\sum_{=1}^{n}\sum_{j=1}^{n} w_{ij}(x_i - \bar{x})(x_j - \bar{x})}{\sum_{i=1}^{n}(x_i - \bar{x})^2}$$

where w_{ij} represents the weights assigned to the neighbours of each cell using a custom written R code. We have assumed equal weights to all the immediate neighbours defined as the cells which are in direct contact with the cell of interest. Moran's plot was plotted with the mean intensity of cell of interest on x axis, and the average intensities of its neighbours on y axis. Correlograms were plotted by computing the global Moran's Index at different lag neighbours.

The Local Moran's Index was calculated to determine the spatial autocorrelation of the proteins of interest for every cell and its neighbours which are in direct contact with it using the following definition:

$$I_i = \frac{(x_i - \bar{x})}{\sum_{k=1}^{n} \frac{(x_k - \bar{x})^2}{(n-1)}} \sum_{j=1}^{n} w_{ij}(x_j - \bar{x})$$

where w_{ij} represents the weights assigned to the neighbours of each cell. We assigned equal weights to all the first nearest neighours of a cell. The "localmoran" function in the 'spdep' package in R was used for this purpose. For each cell and its neighbours, based on deviation from the global mean of the protein amount and the value of its local Moran's index, the cells were classified into four categories "High-High", "High-Low", "Low-High" and "Low-Low", while insignificant deviations were marked as such and were plotted in the form of a LISA[28] cluster map. To assess statistical significance, we used 999 Monte carlo simulations and used a p-value cutoff of 0.05. To capture the spatial clusters to its complete extent of the LISA Actin clusters, cells that are immediate neighbours to the High-High and Low-Low clusters have been represented with darker shades , since LISA analysis only captures the core of spatial clusters[67].

Dynamic heterogeneity domains:

To identify the fast and slow regions of dynamic heterogeneity, we used LISA clustering. 'Low-low' clusters were determined to be the slow regions of dynamic heterogeneity, and 'High-High' clusters were determined to be the fast regions of dynamic heterogeneity.

Mean square displacement:

$$MSD(\Delta t) = \langle | r_i(t + \Delta t) - r_i(t) |^2 \rangle$$

Overlap function:

$$Q(\Delta t) = \langle \frac{1}{N} \sum_{i=1}^{N} W(a - |r_i(t + \Delta t) - r_i(t)|) \rangle$$

As there are cell divisions in both experiment and simulation, we only consider those cells that are present at both t and $t + \Delta t$ when we calculate the MSD and Q(t). Here, angular brackets denote average over t and ensembles (in simulation). For Fig. 2f, $a = 3.25\ \mu m$. For Fig. 3f, $a = 10\ \mu m$. For simulation, $a = 0.1$.

Actin signals:
Actin timeseries signals were obtained from the fluorescence intensity of LifeAct-GFP images by coarse-graining the image with grid sizes comparable to cell size, i.e 30µm, using custom-written python code, from confluent monolayers. For Actin signals from single LifeAct-MDCK cells without any neighbours, per cell intensity was obtained by cell segmentation followed by measuring mean intensity within the cell outline determined by Trackmate.

Particle Image Velocimetry: To compute PIV, iterative PIV using FTTC registration method was computed using the MATLAB toolbox PIVlab[68]. Grid sizes were chosen based on cell size.

Relative cell pressure analysis: Relative cell pressures were computed using Bayesian Force inference[69] adapted using custom code for 2D monolayer data, based on the principle of balancing forces at cell vertices.

Timeseries analysis
Pyboat:
PyBoat[70] is python-based fully automatic stand-alone software that integrates multiple steps of non-stationary oscillatory time series analysis which is being used for the quantification of biochemical and physical heterogeneity spatiotemporally. Pyboat implements continuous wavelet analysis using a sliding Morlet wavelet of different frequencies and determines the power for different frequencies at each time. Then, the main oscillatory component is determined from the heatmap of frequency power at different times and frequency. It also provides optimized detrending, amplitude removal, spectral analysis, ridge detection, oscillatory parameters readout and visualization plots along with an integrated batch-processing option. Using the batch processing option, we also get the most dominant time period of all the spatial positions in the time-series. Using pyboat, we sinc-detrended the Actin time-series signal to obtain the detrended signal ,with detrending period taken to be the imaging duration to remove the trend of increasing Actin with increasing time due to increasing density.

Statistical analysis:
Statistical analyses were performed by Unpaired t-test with Welch's correction using GraphPad Prism 10, unless otherwise mentioned. All experiments were repeated at least three times. Lines represent the median in scatter bar plots unless otherwise mentioned. In violin plot, top line represents 75th percentile, middle line represents the median and the bottom line represents the 25th percentile.

References:

1. Debenedetti, P. G. & Stillinger, F. H. Supercooled liquids and the glass transition. *Nature* **410**, 259–267 (2001).
2. Berthier, L. *Dynamical Heterogeneities in Glasses, Colloids, and Granular Media*. (OUP Oxford, 2011).
3. Berthier, L. & Biroli, G. Theoretical perspective on the glass transition and amorphous materials. *Rev. Mod. Phys.* **83**, 587–645 (2011).
4. Janssen, L. M. C. Active glasses. *J. Phys. Condens. Matter* **31**, 503002 (2019).
5. Berthier, L., Flenner, E. & Szamel, G. Glassy dynamics in dense systems of active particles. *J. Chem. Phys.* **150**, 200901 (2019).
6. Berthier, L., Flenner, E. & Szamel, G. How active forces influence nonequilibrium glass transitions. *New J. Phys.* **19**, 125006 (2017).
7. Angelini, T. E. *et al.* Glass-like dynamics of collective cell migration. *Proc. Natl. Acad. Sci.* **108**, 4714–4719 (2011).
8. Park, J.-A. *et al.* Unjamming and cell shape in the asthmatic airway epithelium. *Nat. Mater.* **14**, 1040–1048 (2015).
9. Malinverno, C. *et al.* Endocytic reawakening of motility in jammed epithelia. *Nat. Mater.* **16**, 587–596 (2017).
10. Garcia, S. *et al.* Physics of active jamming during collective cellular motion in a monolayer. *Proc. Natl. Acad. Sci.* **112**, 15314–15319 (2015).
11. Smeets, B. *et al.* Compaction Dynamics during Progenitor Cell Self-Assembly Reveal Granular Mechanics. *Matter* **2**, 1283–1295 (2020).
12. Ilina, O. *et al.* Cell–cell adhesion and 3D matrix confinement determine jamming transitions in breast cancer invasion. *Nat. Cell Biol.* **22**, 1103–1115 (2020).

614 13. Mongera, A. *et al.* A fluid-to-solid jamming transition underlies vertebrate body axis
615 elongation. *Nature* **561**, 401–405 (2018).
616 14. Schötz, E.-M., Lanio, M., Talbot, J. A. & Manning, M. L. Glassy dynamics in three-
617 dimensional embryonic tissues. *J. R. Soc. Interface* **10**, 20130726 (2013).
618 15. Atia, L. & Fredberg, J. J. A life off the beaten track in biomechanics: Imperfect elasticity,
619 cytoskeletal glassiness, and epithelial unjamming. *Biophys. Rev.* **4**, 041304 (2023).
620 16. Vishwakarma, M. & Di Russo, J. Why does epithelia display heterogeneity? Bridging
621 physical and biological concepts. *Biophys. Rev.* **11**, 683–687 (2019).
622 17. Matoz-Fernandez, D. A., Martens, K., Sknepnek, R., Barrat, J. L. & Henkes, S. Cell division
623 and death inhibit glassy behaviour of confluent tissues. *Soft Matter* **13**, 3205–3212 (2017).
624 18. Malmi-Kakkada, A. N., Li, X., Samanta, H. S., Sinha, S. & Thirumalai, D. Cell Growth Rate
625 Dictates the Onset of Glass to Fluidlike Transition and Long Time Superdiffusion in an
626 Evolving Cell Colony. *Phys. Rev. X* **8**, 021025 (2018).
627 19. Berthier, L., Flenner, E. & Szamel, G. How active forces influence nonequilibrium glass
628 transitions. *New J. Phys.* **19**, 125006 (2017).
629 20. Tjhung, E. & Berthier, L. Discontinuous fluidization transition in time-correlated assemblies
630 of actively deforming particles. *Phys. Rev. E* **96**, 050601 (2017).
631 21. Czajkowski, M., M. Sussman, D., Cristina Marchetti, M. & Lisa Manning, M. Glassy
632 dynamics in models of confluent tissue with mitosis and apoptosis. *Soft Matter* **15**, 9133–
633 9149 (2019).
634 22. Ranft, J. *et al.* Fluidization of tissues by cell division and apoptosis. *Proc. Natl. Acad. Sci.*
635 **107**, 20863–20868 (2010).

23. Sadhukhan, S., Dey, S., Karmakar, S. & Nandi, S. K. A perspective on active glassy dynamics in biological systems. *Eur. Phys. J. Spec. Top.* **233**, 3193–3224 (2024).
24. Sadhukhan, S., Dasgupta, C. & Nandi, S. K. Growing length and time scales in activity-mediated glassy dynamics in confluent cell monolayers. *Phys. Rev. E* **111**, 054416 (2025).
25. Atia, L. *et al.* Geometric constraints during epithelial jamming. *Nat. Phys.* **14**, 613–620 (2018).
26. Pandey, S. *et al.* The structure-dynamics feedback mechanism governs the glassy dynamics in epithelial monolayers. *Soft Matter* **21**, 269–276 (2025).
27. Sadhukhan, S. & Nandi, S. K. On the origin of universal cell shape variability in confluent epithelial monolayers. *eLife* **11**, e76406 (2022).
28. Anselin, L. Local Indicators of Spatial Association—LISA. *Geogr. Anal.* **27**, 93–115 (1995).
29. Sknepnek, R., Djafer-Cherif, I., Chuai, M., Weijer, C. & Henkes, S. Generating active T1 transitions through mechanochemical feedback. *eLife* **12**, e79862 (2023).
30. Ioratim-Uba, A. Mechanochemical Active Feedback Generates Convergence Extension in Epithelial Tissue. *Phys. Rev. Lett.* **131**, (2023).
31. Abhishek, M., Dhanuka, A., Banerjee, D. S. & Rao, M. Excitability and travelling waves in renewable active matter. Preprint at https://doi.org/10.48550/arXiv.2503.19687 (2025).
32. Farhadifar, R., Röper, J.-C., Aigouy, B., Eaton, S. & Jülicher, F. The Influence of Cell Mechanics, Cell-Cell Interactions, and Proliferation on Epithelial Packing. *Curr. Biol.* **17**, 2095–2104 (2007).
33. Barton, D. L., Henkes, S., Weijer, C. J. & Sknepnek, R. Active Vertex Model for cell-resolution description of epithelial tissue mechanics. *PLOS Comput. Biol.* **13**, e1005569 (2017).

659 34. Boocock, D. Interplay between Mechanochemical Patterning and Glassy Dynamics in
660 Cellular Monolayers. *PRX Life* **1**, (2023).
661 35. Boocock, D., Hino, N., Ruzickova, N., Hirashima, T. & Hannezo, E. Theory of
662 mechanochemical patterning and optimal migration in cell monolayers. *Nat. Phys.* **17**, 267–
663 274 (2021).
664 36. Dewan, P., Mondal, S. & Sarkar, S. Oscillation death by mechanochemical feedback.
665 Preprint at https://doi.org/10.48550/arXiv.2504.19655 (2025).
666 37. Mendoza, M. C., Vilela, M., Juarez, J. E., Blenis, J. & Danuser, G. ERK reinforces actin
667 polymerization to power persistent edge protrusion during motility. *Sci. Signal.* **8**, ra47–ra47
668 (2015).
669 38. Tanimura, S. & Takeda, K. ERK signalling as a regulator of cell motility. *J. Biochem.*
670 *(Tokyo)* **162**, 145–154 (2017).
671 39. Lavoie, H., Gagnon, J. & Therrien, M. ERK signalling: a master regulator of cell behaviour,
672 life and fate. *Nat. Rev. Mol. Cell Biol.* **21**, 607–632 (2020).
673 40. LEINWEBER, B. D., LEAVIS, P. C., GRABAREK, Z., WANG, C.-L. A. & MORGAN, K.
674 G. Extracellular regulated kinase (ERK) interaction with actin and the calponin homology
675 (CH) domain of actin-binding proteins. *Biochem. J.* **344**, 117–123 (1999).
676 41. Barros, J. C. & Marshall, C. J. Activation of either ERK1/2 or ERK5 MAP kinase pathways
677 can lead to disruption of the actin cytoskeleton. *J. Cell Sci.* **118**, 1663–1671 (2005).
678 42. Hirashima, T., Hino, N., Aoki, K. & Matsuda, M. Stretching the limits of extracellular
679 signal-related kinase (ERK) signaling - Cell mechanosensing to ERK activation. *Curr. Opin.*
680 *Cell Biol.* **84**, 102217 (2023).

681 43. Kholodenko, B. N., Hancock, J. F. & Kolch, W. Signalling ballet in space and time. *Nat.*
682 *Rev. Mol. Cell Biol.* **11**, 414–426 (2010).
683 44. Shankaran, H. *et al.* Rapid and sustained nuclear–cytoplasmic ERK oscillations induced by
684 epidermal growth factor. *Mol. Syst. Biol.* **5**, 332 (2009).
685 45. Waters, K. M., Cummings, B. S., Shankaran, H., Scholpa, N. E. & Weber, T. J. ERK
686 Oscillation-Dependent Gene Expression Patterns and Deregulation by Stress Response.
687 *Chem. Res. Toxicol.* **27**, 1496–1503 (2014).
688 46. Beta, C. & Kruse, K. Intracellular Oscillations and Waves. *Annu. Rev. Condens. Matter*
689 *Phys.* **8**, 239–264 (2017).
690 47. Ganesan, A. *et al.* Oscillatory signal decoding within the ERK cascade. 2025.07.24.666680
691 Preprint at https://doi.org/10.1101/2025.07.24.666680 (2025).
692 48. Staple, D. B. *et al.* Mechanics and remodelling of cell packings in epithelia. *Eur. Phys. J. E*
693 *Soft Matter* **33**, 117–127 (2010).
694 49. Bi, D., Yang, X., Marchetti, M. C. & Manning, M. L. Motility-Driven Glass and Jamming
695 Transitions in Biological Tissues. *Phys. Rev. X* **6**, 021011 (2016).
696 50. Matoz-Fernandez, D. A. Nonlinear Rheology in a Model Biological Tissue. *Phys. Rev. Lett.*
697 **118**, (2017).
698 51. Nnetu, K. D., Knorr, M., Strehle, D., Zink, M. & Käs, J. A. Directed persistent motion
699 maintains sheet integrity during multi-cellular spreading and migration. *Soft Matter* **8**, 6913–
700 6921 (2012).
701 52. Giavazzi, F., Malinverno, C., Scita, G. & Cerbino, R. Tracking-Free Determination of
702 Single-Cell Displacements and Division Rates in Confluent Monolayers. *Front. Phys.* **6**,
703 (2018).

704 53. Lin, S.-Z. *et al.* Universal Statistical Laws for the Velocities of Collective Migrating Cells.
705 *Adv. Biosyst.* **4**, 2000065 (2020).
706 54. Kim, J. H. *et al.* Unjamming and collective migration in MCF10A breast cancer cell lines.
707 *Biochem. Biophys. Res. Commun.* **521**, 706–715 (2020).
708 55. Vishwakarma, M., Thurakkal, B., Spatz, J. P. & Das, T. Dynamic heterogeneity influences
709 the leader–follower dynamics during epithelial wound closure. *Philos. Trans. R. Soc. B Biol.*
710 *Sci.* **375**, 20190391 (2020).
711 56. Das, J. *et al.* Digital Signaling and Hysteresis Characterize Ras Activation in Lymphoid
712 Cells. *Cell* **136**, 337–351 (2009).
713 57. Raina, D., Fabris, F., Morelli, L. G. & Schröter, C. Intermittent ERK oscillations
714 downstream of FGF in mouse embryonic stem cells. *Development* **149**, dev199710 (2022).
715 58. Nakayama, K., Satoh, T., Igari, A., Kageyama, R. & Nishida, E. FGF induces oscillations of
716 Hes1 expression and Ras/ERK activation. *Curr. Biol.* **18**, R332–R334 (2008).
717 59. Zehnder, S. M., Suaris, M., Bellaire, M. M. & Angelini, T. E. Cell Volume Fluctuations in
718 MDCK Monolayers. *Biophys. J.* **108**, 247–250 (2015).
719 60. Aratyn-Schaus, Y., Oakes, P. W., Stricker, J., Winter, S. P. & Gardel, M. L. Preparation of
720 Complaint Matrices for Quantifying Cellular Contraction. *J. Vis. Exp.* 2173 (2010)
721 doi:10.3791/2173.
722 61. Tseng, Q. *et al.* Spatial organization of the extracellular matrix regulates cell–cell junction
723 positioning. *Proc. Natl. Acad. Sci.* **109**, 1506–1511 (2012).
724 62. Stringer, C., Wang, T., Michaelos, M. & Pachitariu, M. Cellpose: a generalist algorithm for
725 cellular segmentation. *Nat. Methods* **18**, 100–106 (2021).

63. Waisman, A., Norris, A. M., Elías Costa, M. & Kopinke, D. Automatic and unbiased segmentation and quantification of myofibers in skeletal muscle. *Sci. Rep.* **11**, 11793 (2021).

64. Ershov, D. *et al.* TrackMate 7: integrating state-of-the-art segmentation algorithms into tracking pipelines. *Nat. Methods* **19**, 829–832 (2022).

65. Tinevez, J.-Y. *et al.* TrackMate: An open and extensible platform for single-particle tracking. *Methods* **115**, 80–90 (2017).

66. Moran, P. A. P. The Interpretation of Statistical Maps. *J. R. Stat. Soc. Ser. B Methodol.* **10**, 243–251 (1948).

67. GeoDa : An Introduction to Spatial Data Analysis - Anselin - 2006 - Geographical Analysis - Wiley Online Library. https://onlinelibrary.wiley.com/doi/full/10.1111/j.0016-7363.2005.00671.x.

68. Thielicke, W. & Sonntag, R. Particle Image Velocimetry for MATLAB: Accuracy and enhanced algorithms in PIVlab. *J. Open Res. Softw.* **9**, (2021).

69. Ishihara, S. & Sugimura, K. Bayesian inference of force dynamics during morphogenesis. *J. Theor. Biol.* **313**, 201–211 (2012).

70. Mönke, G., Sorgenfrei, F. A., Schmal, C. & Granada, A. E. *Optimal Time Frequency Analysis for Biological Data - pyBOAT*. http://biorxiv.org/lookup/doi/10.1101/2020.04.29.067744 (2020) doi:10.1101/2020.04.29.067744.

Author contributions

M.V conceived the project. S.M. and M.V. designed experiments. S.M. performed and analyzed all experiments except the traction force microscopy with LifeAct MDCK cells, which was performed by M.B.S. Theoretical model was contributed by S.S. and P.D. T.T. performed the LISA analysis, and T.C. contributed to oscillations analysis using pyBOAT. S.K. and S.K.N. contributed to glassy analysis. Analysis and interpretation of data was done by S.M., P.D., Sd.M., S.S., and M.V. M.V. and S.S. developed and wrote the manuscript with help from S.M. and P.D. All authors read, discussed and commented on the manuscript.

Acknowledgements

We thank Sriram R. Ramaswamy, Saroj K Nandi, Tamal Das and Srikanth Sastry for critical discussions and suggestions. M.V. is a partner group leader of the Max Planck Society (MPG), Germany, which has supported part of this work. This work is also supported by the Infosys foundation, Anusandhan National Research Foundation- previously called the Science and Engineering Research Board (project number: SERB SRG/2022/000534), and Indo German Science and Technology Centre (IGSTC WISER scheme). SS acknowledges funding from IISc, Axis Bank Center for Mathematics and Computing, and a startup grant from SERB-DST (SRG/2022/000163). We also acknowledge intramural funds at IISc Bangalore for providing support towards equipment and facilities and for salaries/fellowships of the authors. S.M. acknowledges funding from Prime Minister's Research Fellowship (PMRF).

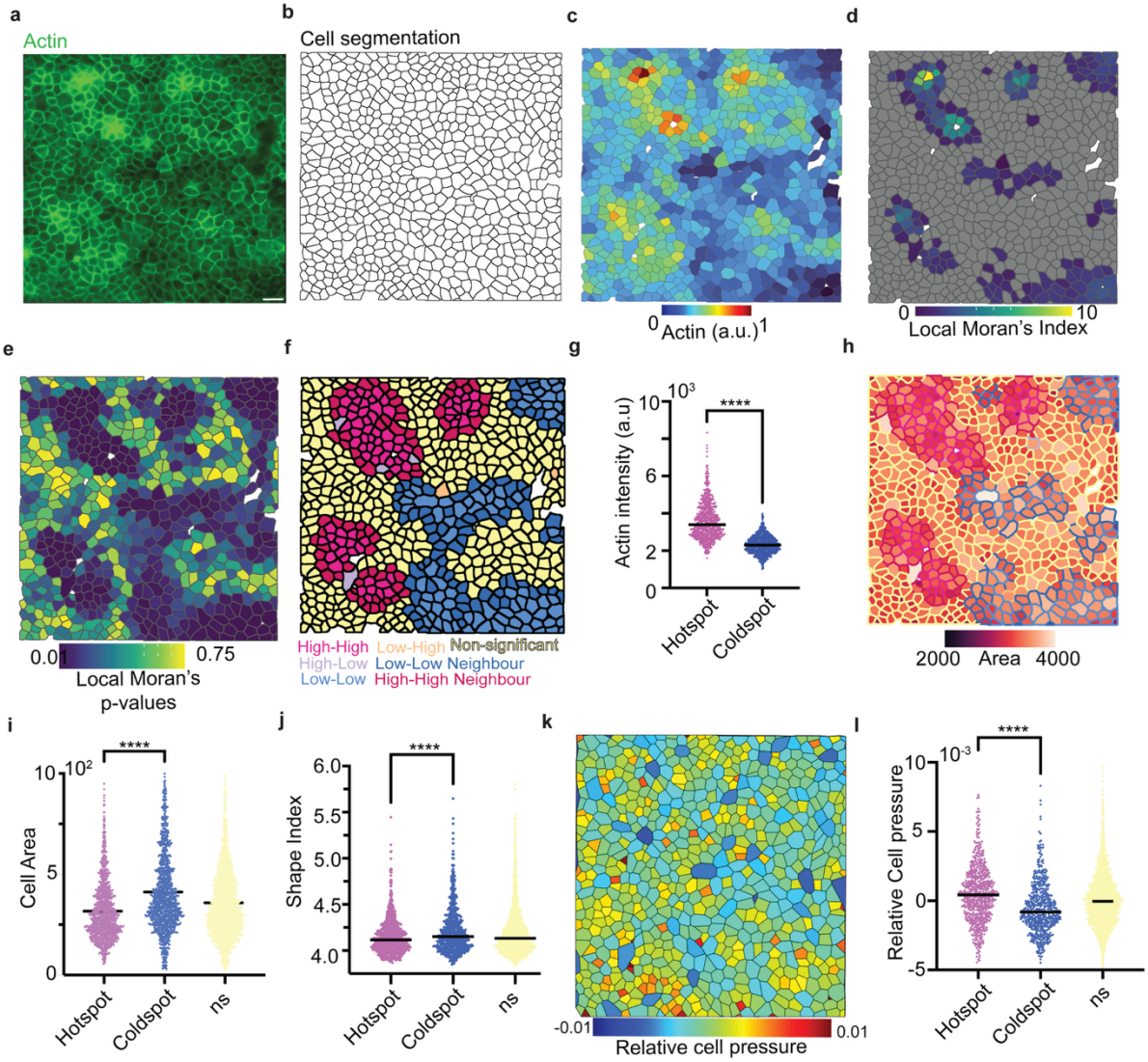

Extended Data Fig 1- Spatial characterization of Actin distribution and Mechanochemical feedback: a) Raw microscopy image of cells stained for Actin with Phalloidin, b) Cell boundaries obtained from cell segmentaion, c) Cells pseudocolored for normalized F-Actin levels, d) Heatmap of Local Moran's Index of cells, e) Heatmap of p-values of cells of Local Moran's Index obtained from , f) LISA cluster map of F-Actin, g) Actin intensity of cells classified as High-High (Hotspots-pink) and Low-Low (Coldspots-blue), h) Cells color-coded for cell area and outlines colored for LISA cluster category, i) Scatter dot plot of single cell area in High-High, Low-Low and Non-significant clusters, j) Scatter dot plot of Shape Index in High-High, Low-Low and Non-significant clusters, k) Heatmap of relative cell pressures obtained by Bayesian Force Inference, l) Scatter dot plot of relative cell pressures in High-High, Low-Low and Non-significant LISA clusters. Scale bars= 50µm. Lines represent the median.

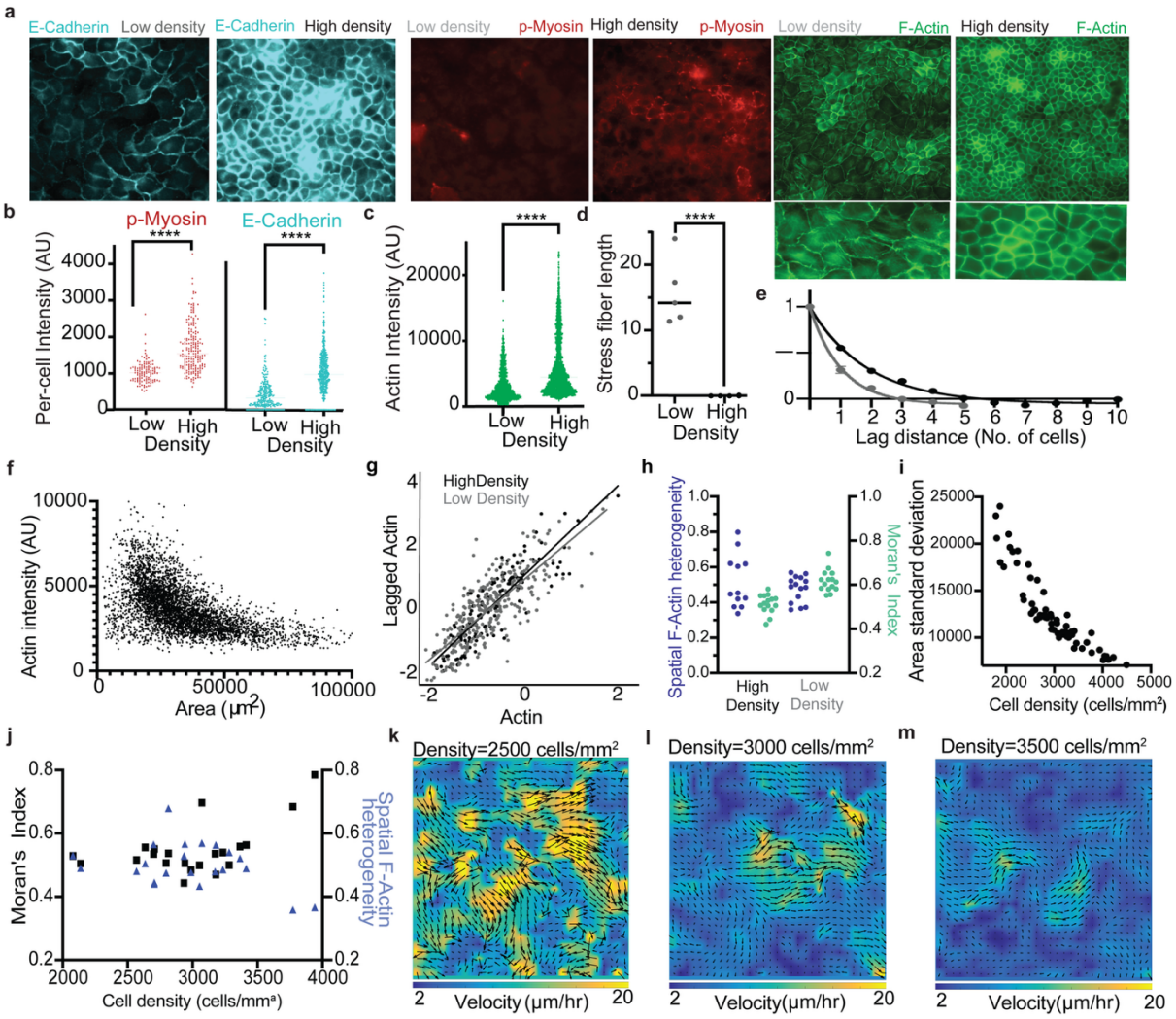

Extended Data Fig 2: Cytoskeletal changes and Moran analysis of loosely and densely packed monolayers: a) Cytoskeletal markers at high (right) and low density (left) obtained by Average Z-projection- (i)- ECadherin ,- (ii)- Phospho-Myosin , - (iii)- F-Actin-top- 2D projection and bottom- Basal F-Actin, b) Myosin and E-Cadherin intensity at low and high density, c) Actin intensity at low and high density, d) Actin stress fiber length at low and high density, e) Correlogram of Moran's index at different neighbour lags, f) Plot of Actin vs Area at low and high density, g) Moran's plot of Actin vs lagged Actin at low and high density, h) Spatial F-Actin heterogeneity (percentage of Non-significant cells) and Global Moran's Index at high and low density, i) Standard deviation of cell area vs density, j) Spatial F-Actin heterogeneity and Moran's Index vs density, k-m) Velocity heatmap from Particle Image Velocimetry map at low (k), medium (l) and high density (m). Scale bars= 50μm. Lines represent the median.

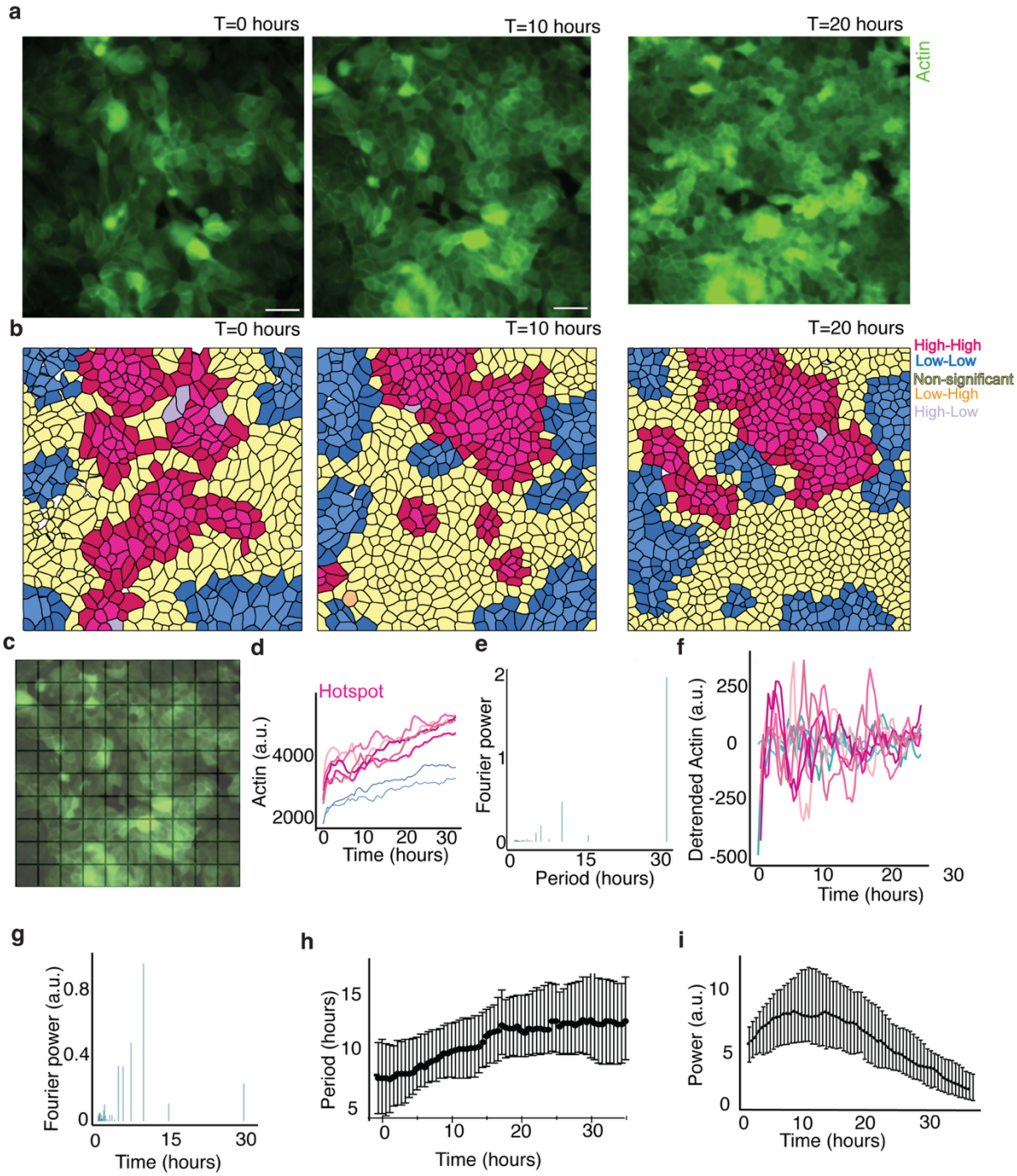

Extended Data figure 3: Analysis of Actin signal from experimental data shows LISA clusters are stable over time and the hotspots and coldspots show oscillations of distinct periods: a) Timelapse images of LifeAct MDCK cells at 0 hours (left), 10 hours (middle), 20 hours (right), and b) Corresponding LISA cluster maps. c) Representative Actin signals from Hotspots (blue) and coldspots (blue), d) Fourier spectrum of a representative Actin signal, e) Representative detrended Actin signals from Hotspots (blue) and coldspots (blue), corresponding to c f) Fourier spectrum of a representative detrended Actin, g-i) Representative detrended Actin signals (top) and corresponding Wavelet plots (bottom), j) Dominant wavelet period over time, k) Dominant

wavelet power over time, l) Phase coherence over time, obtained from Pyboat. Scale bars= 50µm. Lines represent the median.

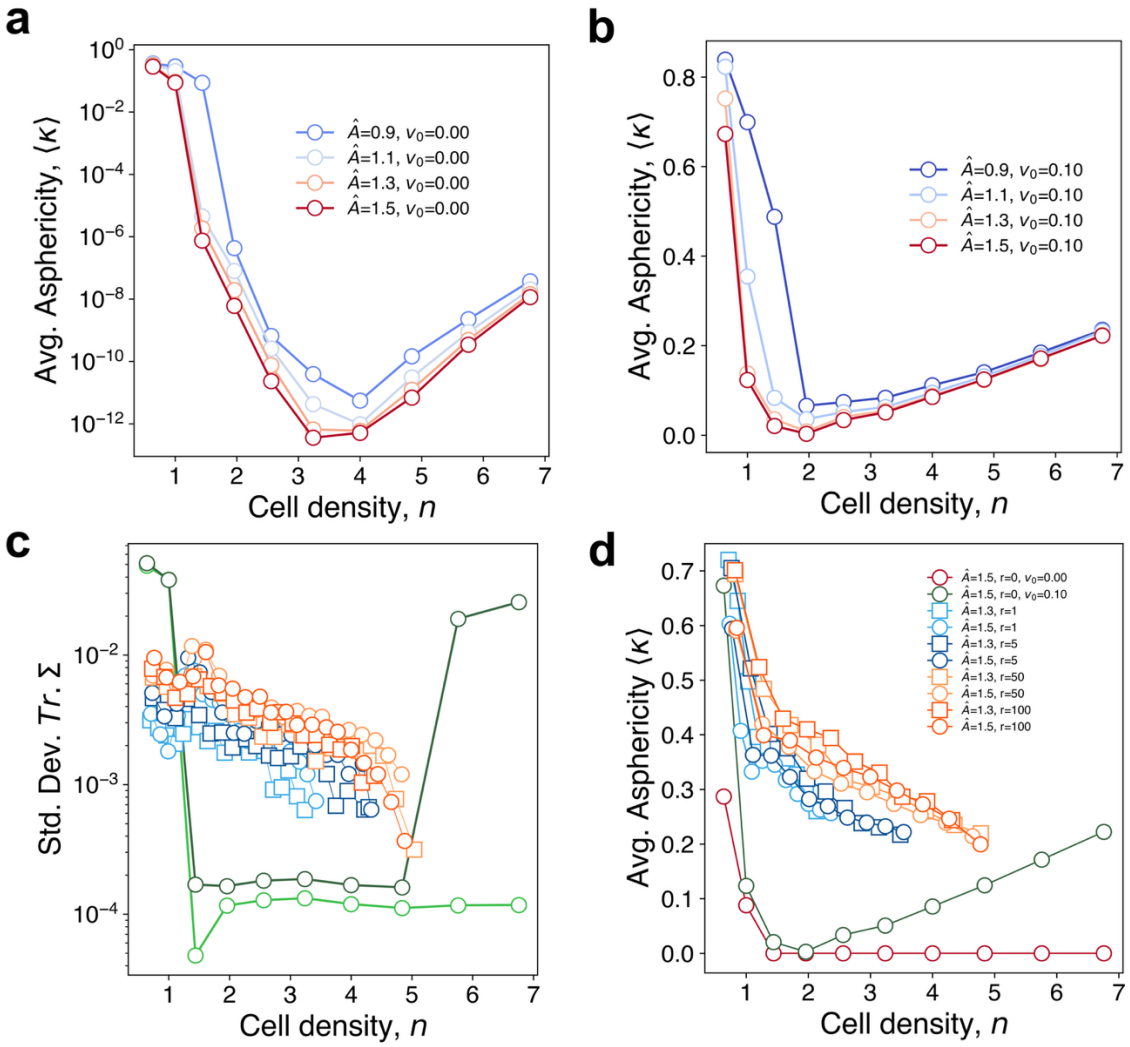

Extended data figure 4: Glass transition in the vertex model: (a) Mean asphericity calculated from quasistatic simulations in the absence of motility shows a discontinuous transition in the mean asphericity near the density at which the mean shape parameter decreases below the jamming threshold (). (b) In the presence of motility, the discontinuity disappears in the quasistatic simulations, but reaches a minimum near the jamming threshold. If the density is decreased at a nonzero division rate, then both (c) stress fluctuation and (d) mean asphericity deviates from the quasistatic trajectories (green markers) and shows clear rate dependence. Higher division rates (orange markers) have higher at the same density than lower division rates (blue markers).

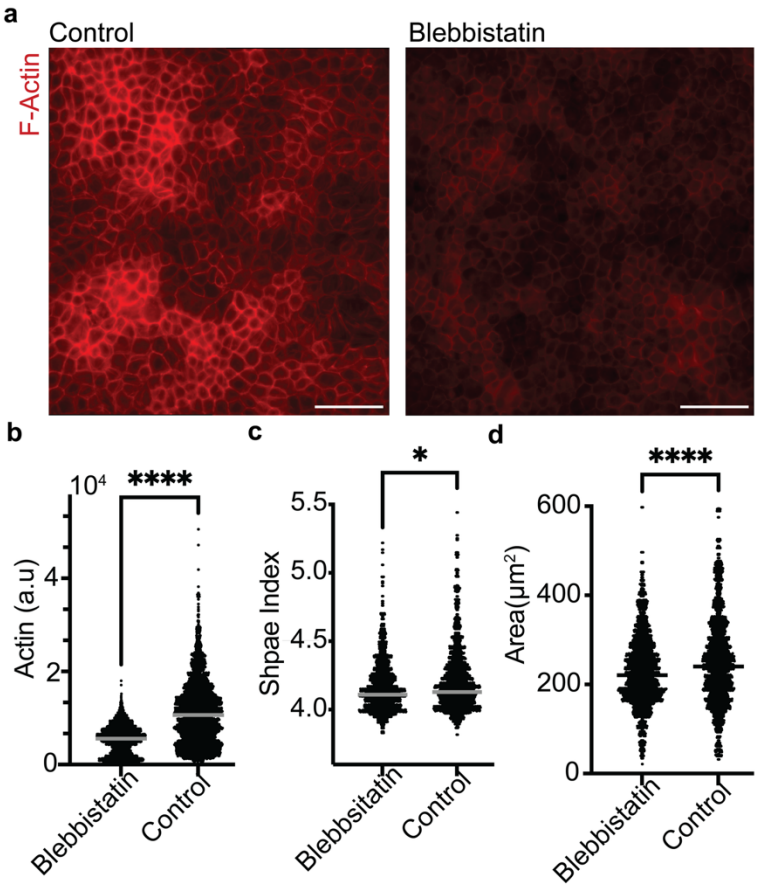

Extended data figure 5: Blebbistatin treatment: a) Left- Control and Right- Blebbistatin treated monolayer, stained for F-Actin with Phalloidin, b) Comparison of Actin levels in Control and Blebbistatin treated monolayers, c) Comparison of Shape Index in Control and Blebbistatin

835

Supplementary Information

Glassy dynamics in active epithelia emerge from an interplay of mechanochemical feedback and crowding

Sindhu Muthukrishnan[1], Phanindra Dewan[2], Tanishq Tejaswi[1], Michelle B Sebastian[1], Tanya Chhabra[1], Soumyadeep Mondal[2], Soumitra Kolya[3], Saroj Kumar Nandi[3], Sumantra Sarkar[2]*, Medhavi Vishwakarma[1]*

1. Department of Bioengineering, Indian Institute of Science, Bangalore, India
2. Department of Physics, Indian Institute of Science, Bangalore, India
3. Tata Institute of Fundamental Research, Hyderabad, India

Correspondence: medhavi@iisc.ac.in and sumantra@iisc.ac.in

Table of contents:

Supplementary Figures 1 to 3 3

Supplementary Movies S1 to S9 6

Supplementary Theory 7

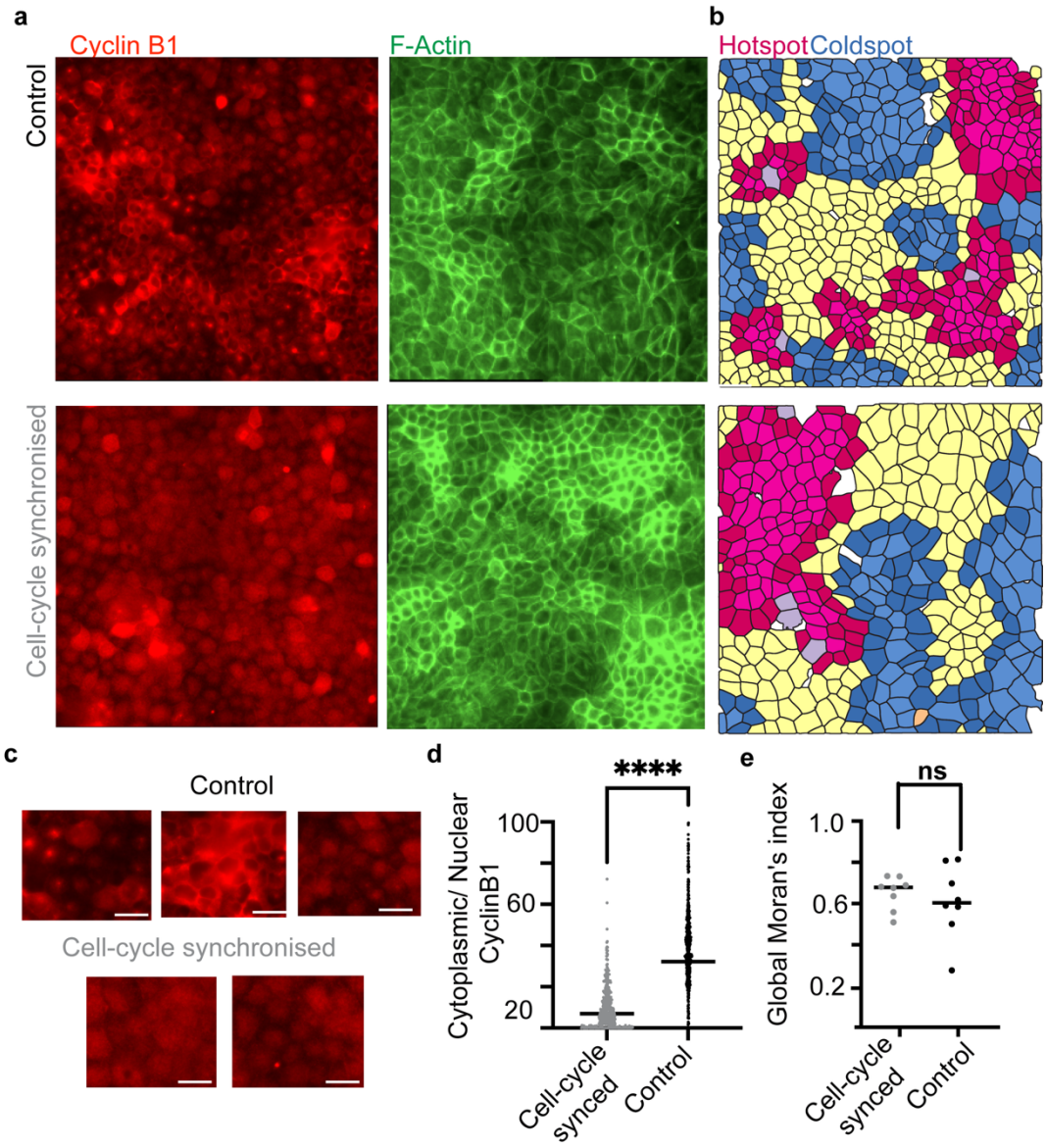

Supplementary figure 1: **Spatial Actin heterogeneity persists after cell cycle synchronization with Thymidine double block:** a) Confluent dishes of MDCK cells stained Cyclin B1 (Left-red) and F-Actin (Right green in cell-cycle synchronized by Thymidine double block (Bottom) and control (Top) samples, b) F-Actin LISA clusters maps corresponding to the images in panel A. c) Zoomed in images of Cyclin B1 corresponding to images in panel A demonstrating nuclear, cytoplasmic, perinuclear distribution of Cyclinb1at different locations in a control monolayer (top), compared to a more uniform distribution in nuclear or cytoplasmic compartments in the cell-cycle synchronized samples. d) Ratio of Cyclin B1 intensity at the nucleus and cytoplasm shows lesser variance in the cell-cycle synchronised samples suggesting uniformity in their cell-cycle state and e) No significant difference in the Global Moran's Index of Control and Cell cycle synchronized samples suggesting that inhomogeneous cell cycle state does not contribute to the observed heterogeneity in Actin levels. Lines represent the median. Scale bars=50µm.

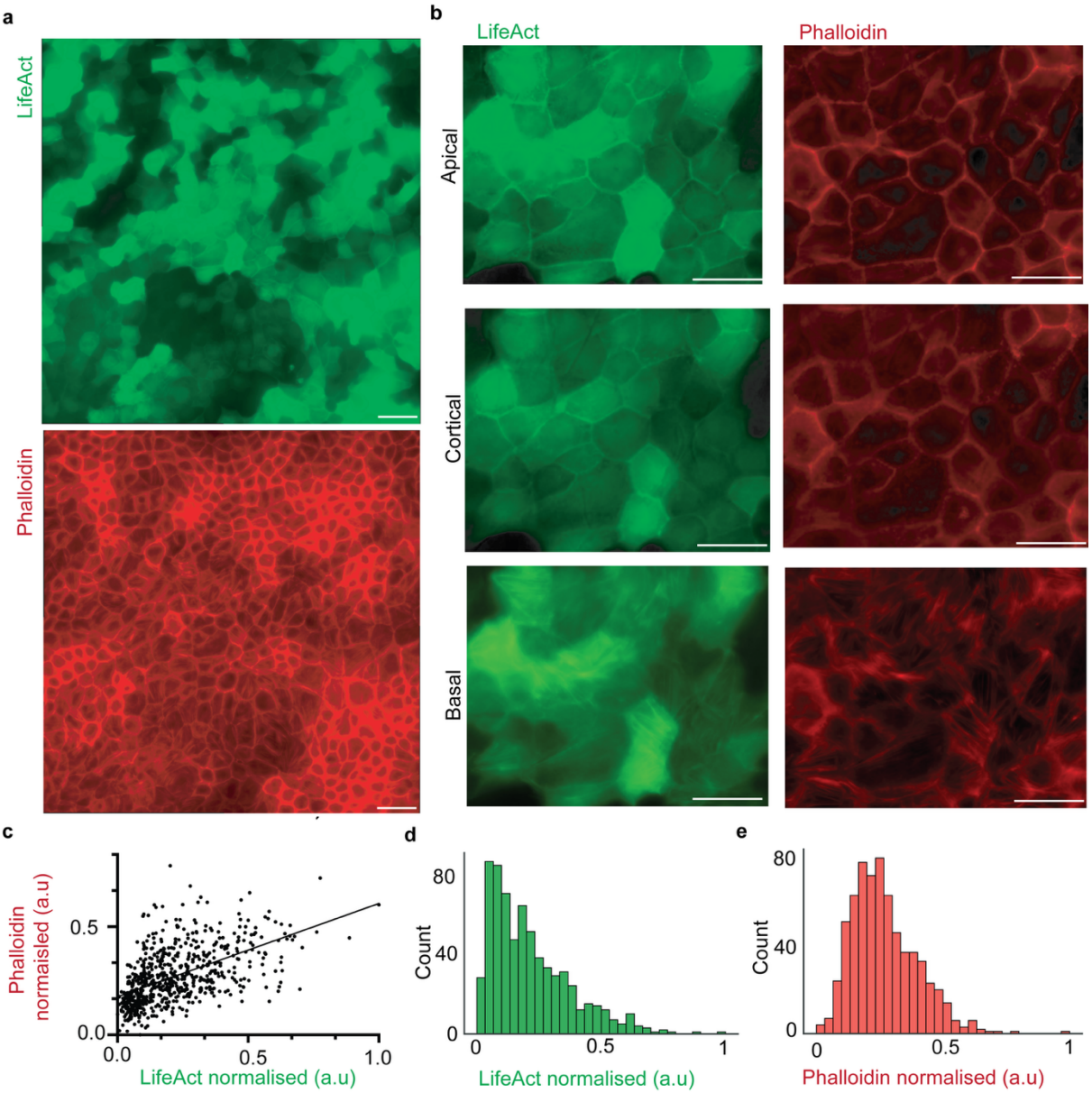

Supplementary figure 2: Comparison of Actin staining with LifeAct and Phalloidin shows similar quanlitative distributions:
Confluent dishes of MDCK cells stained both for LifeAct-GFP (top) and Phalloidin 594 (bottom) imaged in 3D Z-stacks b) Zoomed images of LifeAct (Left-green) and Phalloidin (Right-red) at the top plane (Apical- top), middle plane (Cortical- middle), and bottom plane (Basal plane- bottom), c) Scatter plot of Min-Max Normalised LifeAct and Phalloidin intensities; R^2= 0.2925, d) Histogram of LifeAct and e) Phalloidin intensities. Scale bars=50µm.

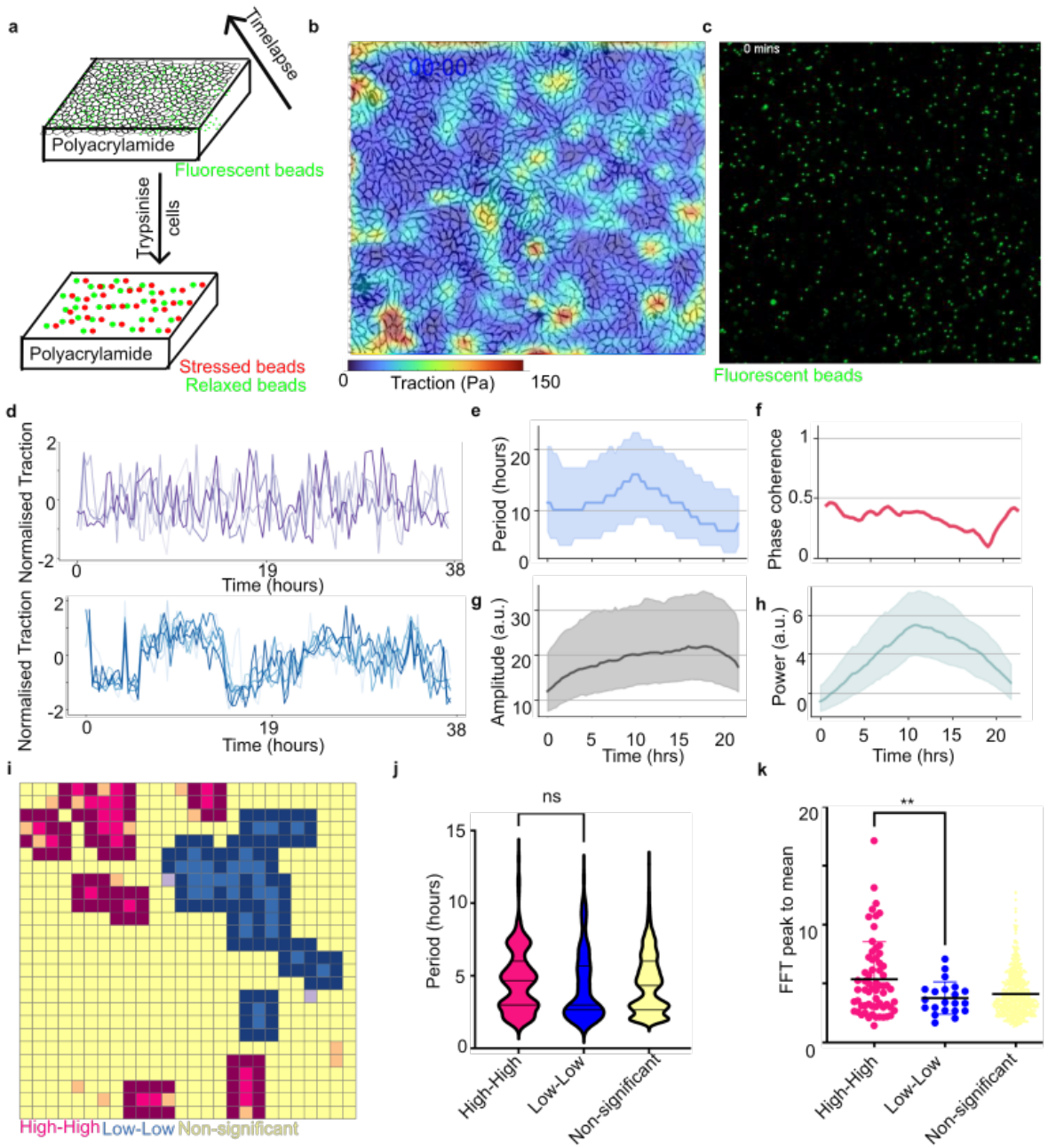

Supplementary Figure 3: Spatiotemporal dynamics of traction force shows hours-scale oscillations: a) Schematic of timelapse traction force Microscopy experiment, b) Traction force heatmap overlaid on cell image, c) Image of beads used in traction force experiment, d) Bottom- Representative locally oscillatory traction signals and top- Representative locally non- oscillatory traction signals, e) Period of oscillation obtained from Wavelet transform using PyBoat, f) Phase coherence over time obtained from Wavelet transform using PyBoat, g) Amplitude of traction signal over time obtained from Wavelet transform using PyBoat, h) Wavelet power over time obtained from Wavelet transform using PyBoat, i) LISA plot of traction force at T=20 hours, j) Plot comparing period of hotspots, coldspots and non-significant regions, k) Plot comparing FFT (Fast Fourier Transform) peak/mean ratio, a metric of oscillation strength at hotspots, coldspots and non-significant regions. Lines represent the median.

Supplementary Video S1: Timelapse movie of homeostatic LifeAct MDCK cells (left) with cell segmentation and tracking (right) used for MSD and Q(t) analysis, imaged every 2.5 minutes. Cell outlines are pseudocoloured for cell area, corresponding to the colourbar in the video. Cell tracks are coloured based on the average track speed, with the cell speed linearly increasing from 2 to 10 μm per hour from blue to red colour. Dark spaces correspond to cells that were not identified during segmentation. Scale bar=50μm.

Supplementary video S2: Timelapse movie of homeostatic LifeAct MDCK cells pseudocoloured for per-cell Actin intensity that were used to analyse the timeperiod of actin clusters. Dark spaces correspond to cells that were not identified during segmentation. Scale bar=50μm.

Supplementary video S3: Timelapse LISA segmentation of Actin intensity- LISA analysis performed for homeostatic LifeAct MDCK cells imaged every 30 minutes. The colours corresponding to LISA classification scheme are as follows: Pink- High-High, Yellow- Non-significant and Blue- Low- Low. Dark spaces correspond to cells that were not identified during segmentation. Scale bar=20μm.

Supplementary video S4: Timelapse movie of homeostatic single cell LifeAct-MDCK cells without cell-cell contacts imaged every two minutes, that were used for the analysis of Actin oscillation period in single cells.

Supplementary video S5: Cell tracking of low (left) and high (right) density monolayers compared side-by-side. The final timepoint shows the tracks for the cells over all timepoints. Cells are pseudocoloured for cell area, corresponding to the colourbar in the video. Cell tracks are coloured based on the average track speed, with the cell speed linearly increasing from 2 to 10 μm per hour from blue to red colour. Scale bar=50μm.

Supplementary Video S6: Experimental videos depicting oscillations of different periods at the actin hotspots and coldspots. Left- Evolution of LISA clusters over time, Middle- Zoomed in view of cells from the coldspots (topleft) and hotspots (bottom left) and corresponding segmented and tracked cells pseudocoloured for Actin intensity (right). Right- Representative detrended Actin signals from coldspots (bottom) and hotspots (top). Scale bar=50μm.

Supplementary Video S7: Simulation video with MCFL-I and MCFL-II shows solidification due to density increase via cell divisions (parameters: $r = 100 \times 10^{-7}, \hat{A} = 1.50$).

Supplementary Video S8: PIV from simulation data shows gradual decrease in cell movement as density increases (parameters: $r = 100 \times 10^{-7}, \hat{A} = 1.50$).

Supplementary Video S9: Simulation video with MCFL-I and MCFL-II showing cells coloured according to the areas (A-1, left) and ERK (E, right) (parameters: $r = 100 \times 10^{-7}, \hat{A} = 1.50$). The system initially shows bistability in areas where cells having $A < 1$ show short period oscillations and cells having $A > 1$ show long period oscillations. The oscillations eventually die out as the system reaches high density and most cells have $A < 1$.

Supplementary Information: Theory

Sindhu Muthukrishnan,[1] Phanindra Dewan,[2] Tanishq Tejaswi,[1] Michelle B Sebastian,[1] Tanya Chhabra,[1] Soumyadeep Mondal,[2] Soumitra Kolya,[3] Saroj Kumar Nandi,[3] Sumantra Sarkar,[2,*] and Medhavi Vishwakarma[1,†]

[1]*Department of Bioengineering, Indian Institute of Science, Bengaluru, Karnataka, India, PIN 560012*
[2]*Department of Physics, Indian Institute of Science, Bengaluru, Karnataka, India, PIN 560012*
[3]*Tata Institute of Fundamental Research, Hyderabad, India, PIN 500046*
(Dated: November 8, 2025)

I. RATIONALE BEHIND THE MODEL AND THE CONSTITUTIVE RELATIONS

A. The canonical vertex model

The canonical vertex model is described by the following hamiltonian [1, 2]:

$$H = \sum_{\alpha} \frac{1}{2} K (A_\alpha - A_0)^2 + \sum_{\alpha} \frac{1}{2} \Gamma P_\alpha^2 + \sum_{i,j} \Lambda_{i,j} l_{i,j}, \tag{S1}$$

where A_α, P_α are the area and perimeter of the cell α. K, Γ, and A_0 are the area elasticity coefficient, perimeter elasticity coefficient, and preferred area of the cells, respectively, which we take to be identical for all the cells. l_{ij} is the length of the interface between cells i and j, and Λ_{ij} is the line tension along this interface. If we assume that the line tension is the same across all the interfaces, such that $\Lambda_{ij} = \Lambda$, the vertex model can be written in another well-known canonical form:

$$H = \sum_{\alpha} \frac{1}{2} K (A_\alpha - A_0)^2 + \sum_{\alpha} \frac{1}{2} \Gamma (P_\alpha - P_0)^2, \tag{S2}$$

where $P_0 = -\Lambda/\Gamma$. The parameters of the vertex model can be normalized to define contractility, $\bar{\Gamma}$ and the normalized tension, $\bar{\Lambda}$ as follows:

$$\begin{aligned} \bar{\Gamma} &= \left(\frac{\Gamma}{K}\right) \frac{1}{A_0} \\ \bar{\Lambda} = \frac{\Lambda}{K A_0^{3/2}} &= -\left(\frac{\Gamma}{K}\right) \frac{P_0}{A_0^{3/2}} \end{aligned} \tag{S3}$$

a. Ground state phase diagram: The ground state of the vertex model has been analyzed from which a phase diagram can be constructed (Fig. T1). We use this phase diagram as a starting point for our analysis.

B. Biological origin of contractility and tension

The actin cytoskeleton of the cell controls the contractility of the cell and the line tension of cell-cell contacts in epithelial tissues. However, they originate from different morphologies of the actin cytoskeleton. Contractility controls the length of the perimeter, and it arises from the formation of contractile actomyosin rings and stress fibers. In contrast, the line tension arises from the accumulation of cortical actomyosin along the cell-cell junctions. Therefore, we can assume that high line tension implies higher accumulation of the branched actin, whereas high contractility implies higher accumulation of the stress fibers and the contractile rings. Translating these observations into the parameters of the vertex model (Eq. S3), we can construct the following picture (Fig. T2). This picture implies that for fixed Γ/K, increasing A_0 decreases the stress fibers and increases the junctional actins. Similarly, an increase in line tension is associated with decreasing P_0 or increasing A_0 or both.

* sumantra@iisc.ac.in
† medhavi@iisc.ac.in

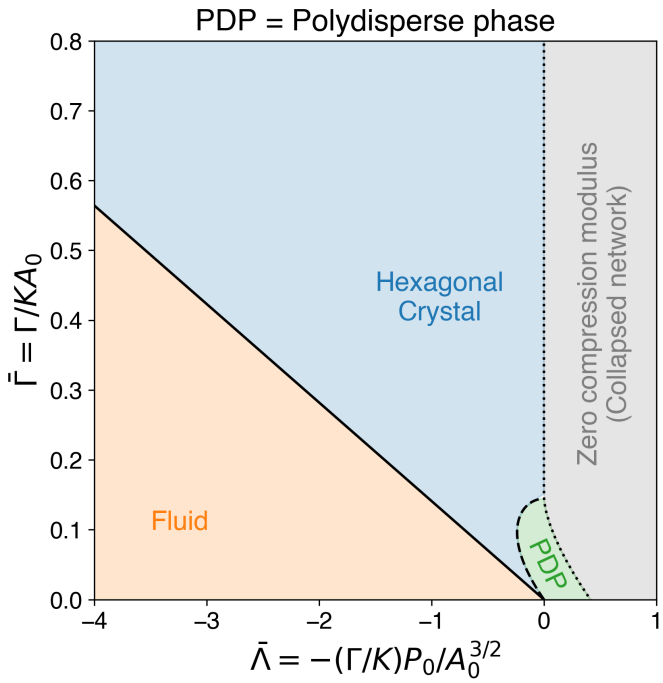

FIG. T1: The ground state phase diagram of the canonical vertex model. The solid and the dashed black lines denote regions where the shear modulus of the hexagonal crystal vanishes. The orange fluid state is composed of soft networks, whereas the green polydisperse phase is composed of polygons of various shapes and sizes. In the canonical vertex model, the PDP can contain 4-8 or 3-12 crystalline lattices.

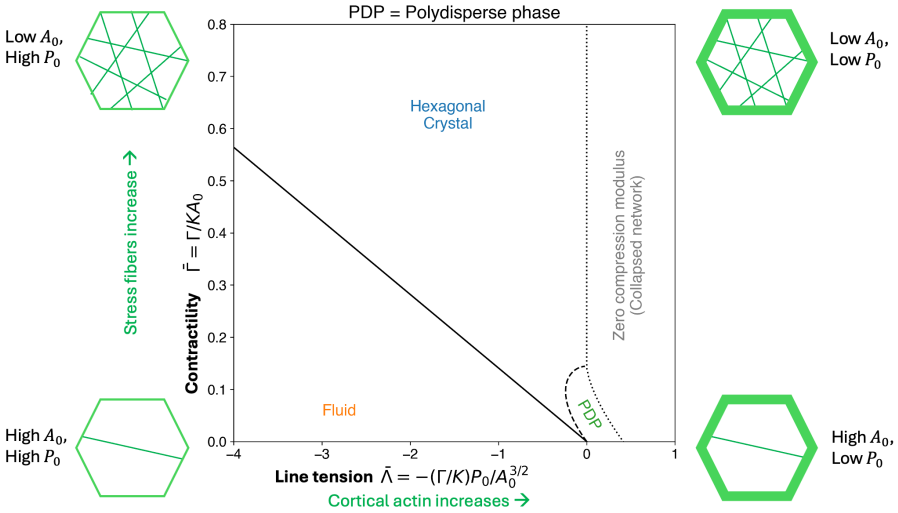

FIG. T2: The biological origin of the contractility and tension.

As a tissue matures through cell division and cell-cell interactions, we expect it to explore some trajectories in this phase diagram. In our experiments, the tissue solidifies through cell division. Time-lapse imaging of actin, myosin, and E-cadherin during this solidification process reveals that the cells contain many elongated stress-fibers and low accumulation of junctional actin at low densities. The opposite trend is seen at high density, in which the cells have highly mature cell-cell junctions with high accumulation of actin, myosin, and E-cadherin at the junctions. In contrast, the actin is highly depleted in the bulk, and stress fibers are hardly seen. Similar observations were also reported earlier. Hence, during tissue solidification through cell division, the trajectory should start at the upper left part of the phase diagram and move to the lower right part, as shown in the figure below (Fig. T3).

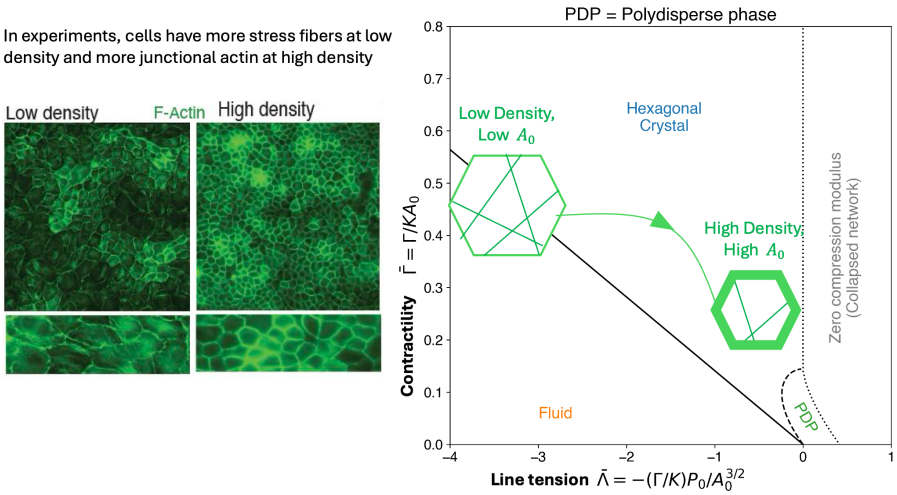

FIG. T3: Trajectory of our experiment on the phase diagram. A theoretical description of tissue solidification through cell division will require a similar change in the contractility and line tension.

C. Constitutive laws for tissue solidification through cell division

Based on the analysis above, it is clear that any model of crowding-induced tissue solidification, such as through cell division, would require constitutive relations that ensure high contractility, low tension at low density, and low contractility and high tension at high density. One way to achieve this phenomenology is to consider the load-dependent binding of myosin to actin.

1. *Load-dependent binding of myosin*

The unbinding rate of myosin from actin depends on the local strain. The higher the contraction of the actomyosin network, the lower the unbinding rate. In fact, to a good approximation, the unbinding rate, k_u, decays exponentially with the strain, ϵ. Specifically, for an isotropic deformation of the cell in the 2D vertex model, the strain is a scalar:

$$\epsilon = \frac{A - \hat{A}}{\hat{A}}, \tag{S4}$$

where $\hat{A}$ is a reference area, whose form will be determined later. The unbinding rate can be written as [3, 4]:

$$k_u = k_u^0 \exp(\chi\epsilon) \tag{S5}$$
$$= k_u^0 \exp\Big(\chi(A/\hat{A} - 1)\Big) \tag{S6}$$
$$\equiv k_u^0 \exp(\chi(x-1)) \tag{S7}$$
$$x = A/\hat{A} \tag{S8}$$

Hence, for $\chi > 0$, which is what is observed experimentally [3, 4], the unbinding rate decreases with increasing contraction, $x < 1$, leading to increased actomyosin binding, which increases the contraction further. This mechanochemical feedback loop, which we call MCFL-I, changes the bound fraction of actomyosin in a density-dependent manner. To see this, consider the following reaction:

$$M + F \underset{k_b}{\overset{k_u}{\rightleftharpoons}} MF \tag{S9}$$

Here M and F denotes myosin and F-actin, respectively, and MF is their bound state. Assuming that the reactions occur at a much faster rate than appreciable changes in the cell area, the bound fraction of myosin can be calculated assuming chemical equilibrium.

$$p_{bound} = \frac{[MF]}{[M] + [MF]} \tag{S10}$$

In chemical equilibrium,

$$k_b[M][F] = k_u[MF] \tag{S11}$$

$$\therefore p_{bound} = \frac{1}{1 + \frac{k_u}{k_b[F]}} \tag{S12}$$

$$= \frac{1}{1 + \frac{k_u^0}{k_b}\frac{\exp[\chi(x-1)]}{[F]}} \tag{S13}$$

$$= \frac{1}{1 + K_D^0\frac{\exp[\chi(x-1)]}{[F]}} \tag{S14}$$

The equation simplifies significantly when $\chi = 1$, and $x \approx 1$. In this limit,

$$p_{bound} \approx \frac{1}{1 + \frac{K_D^0}{N_F/A}x} \tag{S15}$$

$$\tag{S16}$$

where $N_F = [F]A$ is the number of f-actin in the cell. Our experiments show that the total amount of actin remains constant. Hence, K_D^0/N_F is a constant. In fact, we define:

$$\hat{A} = N_F/K_D^0. \tag{S17}$$

Clearly, $\hat{A}$ is inversely proportional to the dissociation constant of the actomyosin complex. Hence, it can be controlled by controlling the binding affinity of the myosin. In general, the lower the dissociation constant, the higher the $\hat{A}$, and hence the higher the binding affinity of myosin to actin. With this definition, we can write the bound fraction as:

$$p_{bound} = \frac{1}{1 + \left(\frac{A}{\hat{A}}\right)^2} = \frac{1}{1 + x^2} \tag{S18}$$

Eq. S18 works remarkably well for a range of area, A (Fig. T4). Furthermore, this formula is much easier to work with in analytical calculations than the more general equation:

$$p_{bound} = \frac{1}{1 + x\exp\{[\chi(x-1)]\}}. \tag{S19}$$

Hence, we use this equation for all our simulations and analytical calculations.

2. *Constitutive relations*

The line tension, $\bar{\Lambda}$ should be proportional to the bound fraction. Because $\bar{\Lambda} \propto -P_0$, P_0 should decrease with p_{bound}, the fraction of myosin bound with branched actin. p_{bound} increases with decreasing area, that is, increasing density. Because the number of stress fibers decreases with increasing cell density, we expect the number of stress fibers to decrease with increasing p_{bound}. This reduction in stress fiber arises from the conservation of the total actin in the cell and allocation of more F-actin into the cell-cell junctions as the density increases. This observation implies that contractility, $\bar{\Gamma}$, should decrease with increasing p_{bound}. Finally, because $\bar{\Gamma} \propto 1/A_0$, A_0 should increase with p_{bound}. Taken together, we propose the following constitutive relations:

$$\begin{aligned} A_0(A) &= 2a_0\frac{1}{1 + \left(\frac{A}{\hat{A}}\right)^2} \\ P_0(A) &= 2\hat{q}_0\sqrt{a_0}\frac{\left(\frac{A}{\hat{A}}\right)^2}{1 + \left(\frac{A}{\hat{A}}\right)^2}. \end{aligned} \tag{S20}$$

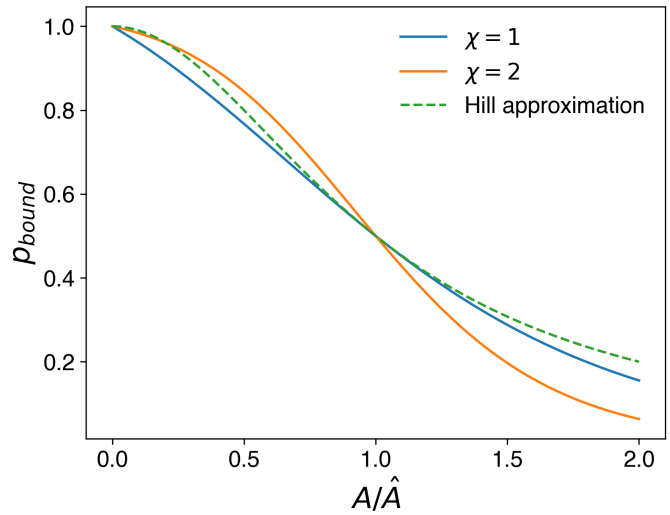

FIG. T4: Comparison of p_{bound} computed from the true expression (Eq.S19) vs the hill approximation (Eq.S18).

Here,

$$a_0 = A_0(\hat{A}) = 1 \tag{S21}$$

$$\hat{q_0} = P_0(\hat{A})/\sqrt{A_0(\hat{A})} \tag{S22}$$

$$\text{Cell Density, } n = 1/A \tag{S23}$$

These constitutive relations, shown in Fig. T5, reproduce the experimentally observed behavior with fluid phase at low densities and crystalline phase at high densities, as shown in Fig. T6. In the next section, we will use them to construct the ground state phase diagram as a function of cell density. However, it is important to consider alternate constitutive relations, which we do next.

D. Alternate constitutive relations

1. *Constant A_0 and P_0, but density-dependent Γ/K*

If A_0 and P_0 are constants, then a simple linear relationship exists between $\bar{\Gamma}$ and $\bar{\Lambda}$:

$$\bar{\Lambda} = -\left(\frac{\Gamma}{K}\right)\frac{P_0}{A_0^{3/2}} = -\frac{P_0}{\sqrt{A_0}}\frac{\Gamma}{KA_0} \tag{S24}$$

$$\therefore \bar{\Lambda} = -\hat{q}_0\bar{\Gamma}. \tag{S25}$$

The line separating the fluid region from the hexagonal crystal in Fig. T1 satisfies the equation:

$$\bar{\Lambda} = -4\sqrt{\pi}\bar{\Gamma}. \tag{S26}$$

Hence, as long as the shape parameter $\hat{q}_0 < 4\sqrt{\pi} \approx 7.1$, the trajectory always remains in the crystalline region. Conversely, if $\hat{q}_0 > 4\sqrt{\pi}$, then the trajectory strictly remains in the fluid region of the phase diagram. For sufficiently small $\hat{q}_0$, the trajectories in the crystalline phase can reach the PDP phase at small $\bar{\Gamma}$ values. Clearly, this protocol does not match experimental observation, where a single trajectory remains in the fluid phase at a low density and reaches the crystalline phase at high density. Doing so requires both $\bar{\Gamma}$ and $\hat{q}_0$ to change with density, in which case, they are equivalent to the constitutive relations Eq. S20.

2. *$A_0 \propto 1/n$, P_0 and Γ/K constant*

As cell density, n, increases, the area of the cells, A, decreases. The average area scales as $1/n$. One possible way to achieve this is to make the preferred area, $A_0 = 1/n$, while keeping all other parameters constant. Hence, in this

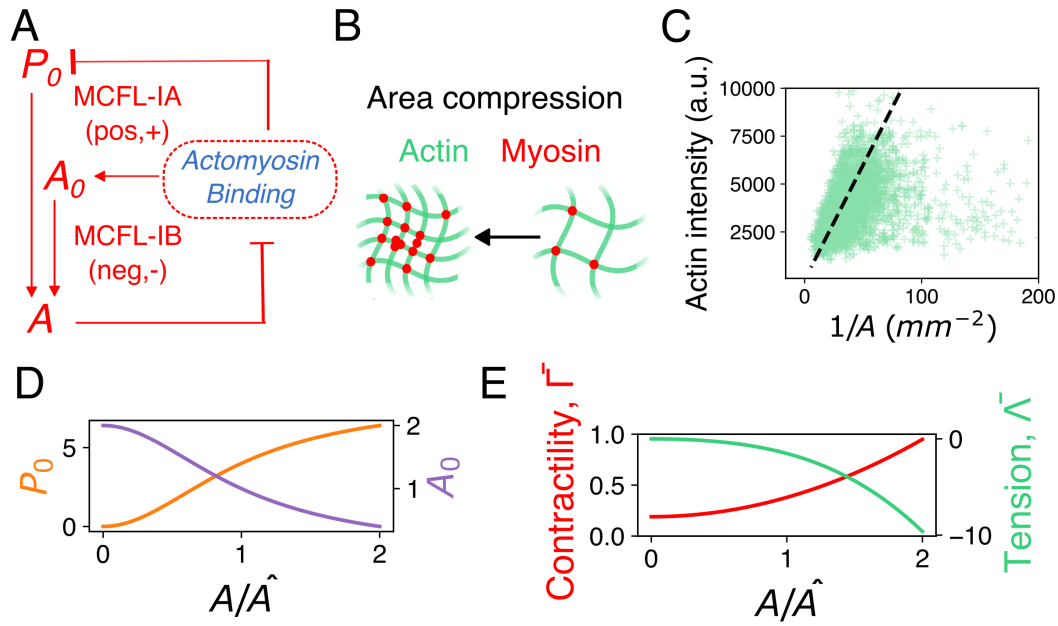

FIG. T5: (A)MCFL-I consists of two interacting positive and negative feedback loops. MCFL-IA leads to bistability, which creates coexisting cells with larger and smaller areas. MCFL-IB stabilizes the bistable areas from increasing or decreasing indefinitely, creating a stable distribution of cells even at high densities. (B) It arises from the load-dependent binding of myosin to actin. (C) Actin intensity is inversely proportional to the area of the cell, implying that the total actin is constant. (D) A_0 and P_0 as a function of $A/\hat{A}$ shows the density-dependence of the constitutive relations. (E) Contractility and tension as a function of $A/\hat{A}$ computed from these constitutive relations.

protocol, the contractility, $\bar{\Gamma}$, increases with n, and the line tension decreases with n, leading to fluidization at high density. Furthermore, the trajectory is exactly opposite to what is observed in experiments, including ours. Hence, this constitutive relation is unphysical and should not be used to model a proliferating tissue.

II. GROUND STATE PHASE DIAGRAM OF THE VERTEX MODEL WITH MCFL-I

A. Solid-Fluid phase transition at low density

In the hexagonal ground state of the vertex model, the shear modulus is given by [1, 2]:

$$\bar{G} = \frac{\sqrt{3}}{64}\frac{\bar{\Lambda}^2}{\bar{\Gamma}^2} + 2\sqrt{3}\bar{\Gamma} - \frac{1}{2} \tag{S27}$$

The normalized tension, $\bar{\Lambda}$, and normalized contractility, $\bar{\Gamma}$, are functions of the bound fraction p_{bound} through A_0 and P_0. Specifically,

$$z = p_{bound} = \frac{1}{1+(A/\hat{A})^2} \tag{S28}$$

$$\bar{\Gamma} = \frac{\Gamma}{K}\frac{1}{A_0} \tag{S29}$$

$$\bar{\Lambda} = -\frac{\Gamma}{K}\frac{P_0}{A_0^{3/2}} \tag{S30}$$

$$A_0 = 2z \tag{S31}$$

$$P_0 = 2\hat{q}_0(1-z), \tag{S32}$$

where $\hat{q}_0$ is the preferred shape index.

In the canonical vertex model a fluid-to-crystal transition happens when [2]:

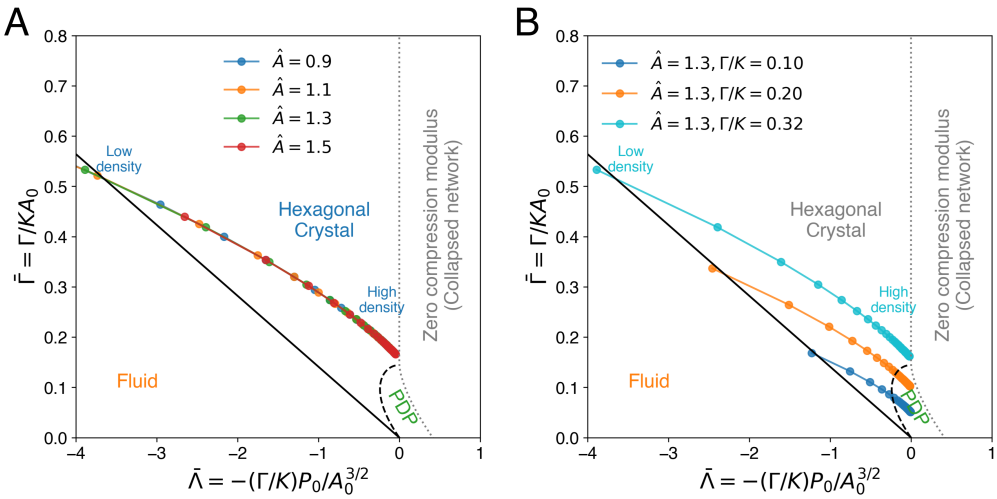

FIG. T6: (A)The constitutive relations (Eq. S20) reproduce density dependence consistent with experimental trajectories. Here, trajectories for a few $\hat{A}$ values are shown. (B) Changing Γ/K shifts these trajectories along the $\bar{\Gamma}$ axis. For $\Gamma/K < 1/2\sqrt{3}$, the trajectories can access the PDP phase at high density. The rigidity of this state is yet to be determined.

$$\bar{\Lambda} = -4\sqrt{\pi}\bar{\Gamma}. \tag{S33}$$

Substituting Eqs. S29- S32 in Eq. S33 we get:

$$z^2 - \left(2 + \frac{8\pi}{\hat{q}_0}\right)z + 1 = 0. \tag{S34}$$

Clearly, the solution of this equation depends only on the shape index $\hat{q}_0$, and the transition from the fluid to solid phase happens at:

$$z_{lo} = \left(1 + \frac{4\pi}{\hat{q}_0}\right) - \sqrt{\frac{8\pi}{\hat{q}_0} + \frac{16\pi^2}{\hat{q}_0^2}} \tag{S35}$$

Using Eq. S28, we can find the area, A_{lo} at which this transition happens. The cell density n_{lo} is then obtained from $1/A_{lo}$.

$$A_{lo} = \hat{A}\sqrt{\frac{1}{z_{lo}} - 1} \tag{S36}$$

$$n_{lo} = 1/A_{lo} = \frac{1}{\hat{A}}\sqrt{\frac{z_{lo}}{1 - z_{lo}}}. \tag{S37}$$

This transition line is marked by the solid black line in Fig. T7.

B. Solid-Fluid phase transition at high density

Interestingly, another solid-fluid transition is possible in the vertex model presented here, which originates from the density-dependence of the parameters P_0 and A_0 through MCFL-I. To show this, we substitute Eqs. S29- S32 in Eq. S27 and set $\bar{G} = 0$. From which we get:

$$az^2 + bz + c = 0 \tag{S38}$$

$$a = \frac{\sqrt{3}\hat{q}_0^2}{32} \tag{S39}$$

$$b = -(2a + 1/2) \tag{S40}$$

$$c = \sqrt{3}\frac{\Gamma}{K} + a. \tag{S41}$$

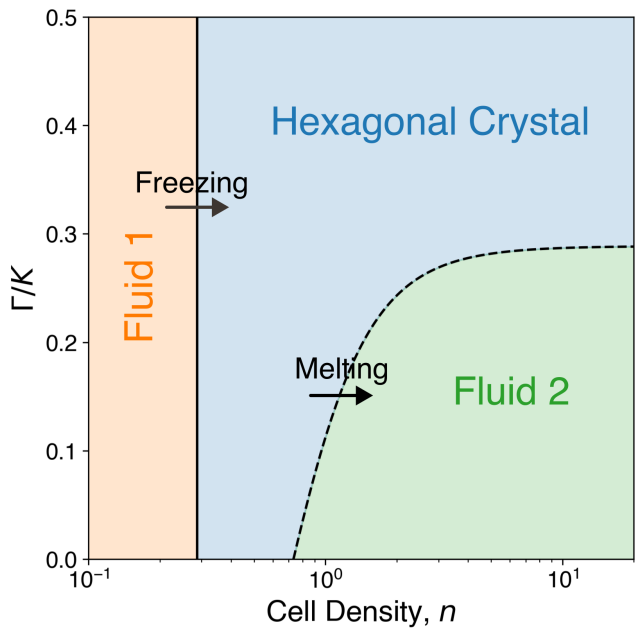

FIG. T7: The ground state phase diagram of the vertex model in the absence of any motility. For $\Gamma/K < 1/2\sqrt{3} \approx 0.29$, the tissue undergoes two solid-fluid phase transitions at a low and a high cell density. Above this threshold, there is only one phase transition at low cell density. Both solid-fluid transitions are discontinuous. The solid-fluid transition at high densities originates from topologically defect-driven 2D melting of the crystalline phase.

Because $b < 0$, only one root lies between 0 and 1, which is what we require for valid solutions of $x = p_{bound}$, and it is:

$$z_{hi} = -\frac{b + \sqrt{b^2 - 4ac}}{2a}. \tag{S42}$$

The condition for validity can be found by setting $z_{hi} = 1$, which yields:

$$\left(\frac{\Gamma}{K}\right)_{max} = \frac{1}{2\sqrt{3}} \approx 0.288675. \tag{S43}$$

For Γ/K below this threshold, the ground state undergoes a fluidity transition at $p_{bound} = z_{hi}$. From which, we find the density, n_{hi}, at which the shear modulus vanishes and the crystal fluidizes.

$$A_{hi} = \hat{A}\sqrt{\frac{1}{z_{hi}} - 1} \tag{S44}$$

$$n_{hi} = 1/A_{hi} = \frac{1}{\hat{A}}\sqrt{\frac{z_{hi}}{1 - z_{hi}}}. \tag{S45}$$

This line corresponds to the black dashed line in the phase diagram shown in Fig. T7. Clearly, n_{hi} diverges at $z_{hi} = 1$, i.e., at $(\Gamma/K)_{max}$. Hence, for $\Gamma/K > (\Gamma/K)_{max}$, the crystal does not fluidize at high densities. In the canonical vertex model phase diagram (Fig. T1), this second fluid region corresponds to the PDP region. From our simulations, we find that the configurations behave like a fluid. Hence, here, instead of PDP, we refer to them as fluid. Finally, in the canonical vertex model, the compression modulus vanishes when $P_0 = 0$, which corresponds to $n = \infty$ in our model.

C. Effect of topological transitions and active forces

The ground state analysis presented here excludes topological transitions, such as cell intercalation through the T1-transitions and the node-switching algorithm used to prevent cell overlaps. Furthermore, we also do not consider

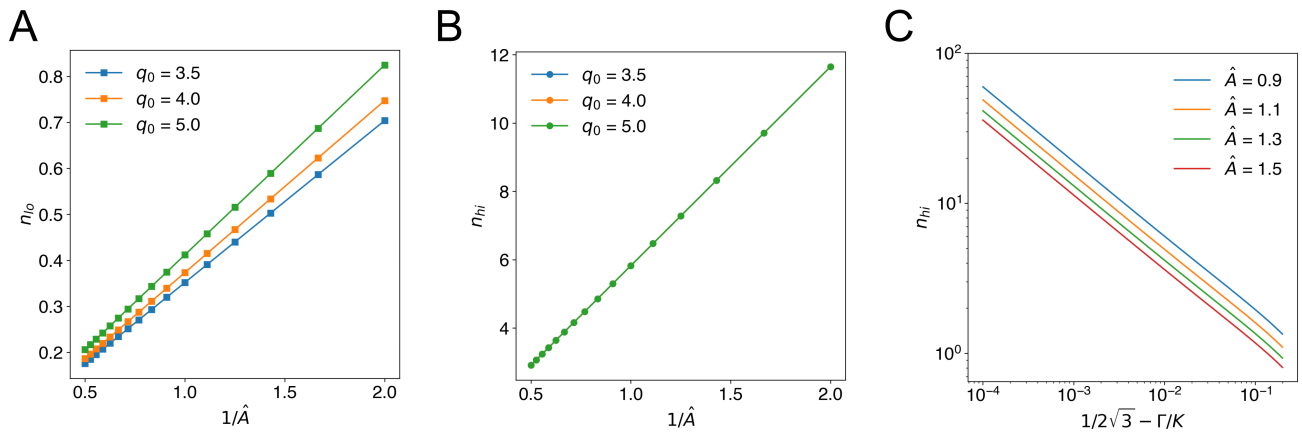

FIG. T8: (A) n_{lo} and (B) n_{hi} vs $1/\hat{A}$ shows the linear dependence of the densities on $\hat{A}$ and weak-dependence on $\hat{q}_0$. (C) n_{hi} scales as $(1/2\sqrt{3} - \Gamma/K)^{-1/2}$.

the effect of active forces, such as from cell motility and MCFL-II, in these calculations. These transitions and forces can perturb the integrity of the crystalline phase, and we expect them to have nontrivial effects on the stability of the phases. While a detailed exploration and characterization of these perturbations is beyond the scope of the current manuscript, here we list our observations on their effects.

1. **Topological transitions and MCFL-II**: We performed a set of simulations in the absence of motility, but with the other perturbations mentioned here. As shown in the main text figures, the phase transitions do not change qualitatively in the presence of these forces. The location of n_{lo} does change. Although the transition to the crystalline state happens at a much larger density (~ 1.5 in practice vs ~ 0.3 from the ground state analysis).

2. **Motility**: Motility can fundamentally change the nature of the phase diagram. For example, in the absence of motility, we observe no fluidization transition at high density in constant density simulations for $\Gamma/K \approx 0.32$, the estimated value for MDCK cells [5]. However, for sufficiently large motility values, the second fluidization transition happens at this Γ/K value.

D. The nature of the fluidization transition at high density

The surprising fluidization transition at high density arises from the 2D melting of the hexagonal crystal through the accumulation of topoplogical defects. Hence, it is a discontinuous melting transition, which we verify through numerical simulation of the system with ($\Gamma/K = 0.32$) and without motility ($\Gamma/K = 0.2$). However, unlike 2D molecular or colloidal systems, the cells in the vertex model do not start freely diffusing as the integrity of the tissue needs to be maintained. Hence, the defects accummulate and increase the stress on the cell monolayer, which can be relieved by out-of-plane buckling. Indeed, such a buckling transition is observed in MDCK tissues at high densities. However, this demonstration is not possible within the current theoretical framework and will be investigated in a future work.

III. NUMERICAL SIMULATION OF THE MODEL

To model the various behaviour seen in experiments done with MDCK cells, we have used an active vertex model with mechanochemical feedback. Another important aspect of the model is the fact that cells can divide in the vertex model. The mechanochemical feedback in our model consists of two mechanochemical feedback loops (MCFLs). Each part of the model will be discussed below.

A. Active Vertex Model

The vertex model represents tissues as a tessellation of polygons, with each polygon representing a cell. The energy of the vertex model for cells labelled by α is written as:

$$E_{VM}(t) = \sum_{\alpha} \left[\frac{K_\alpha}{2}(A_\alpha - A_\alpha^0(t))^2 + \frac{\Gamma_\alpha}{2}(P_\alpha - P_\alpha^0(t))^2 \right] \tag{S46}$$

Here, the area energy comes from the volume incompressibility of cells whereas the perimeter energy term comes from the actomyosin contractility of cells. The constant parameters K_α is the area modulus which gives the area elasticity and Γ_α is the perimeter modulus which is the elasticity due to the actomyosin cortex. The cells can be either solid-like or fluid-like according to the shape index defined as $q = P/\sqrt{A}$.

The vertices in the vertex model undergo overdamped dynamics. So, the equation of motion of the ith cell is given by:

$$\zeta \frac{\partial \vec{r}^{(i)}}{\partial t} = \vec{F}^{(i)} + \vec{F}_{act}^{(i)} + \vec{F}_{motility}^{(i)} \tag{S47}$$

Here, $\vec{r}^{(i)}$ is position of the ith vertex, and $\vec{F}^{(i)}$ is the equilibrium force on each vertex given by the gradient of the vertex model energy: $\vec{F}^{(i)} = -\nabla_{\vec{r}^{(i)}} E_{VM}$. Additionally, there can be other active forces $\vec{F}_{act}^{(i)}$ and motility force $\vec{F}_{motility}^{(i)}$. We have $\vec{F}_{act} = 0$ in our simulations. $\vec{F}_{motility}^{(i)}$ is a force which propels individual cells by $\vec{F}_{motility}^{(i)} = v_0 \vec{p}_\alpha$, where $\vec{p}_\alpha$ is the polarity of a given cell given by $\vec{p}_\alpha = (\cos\theta_\alpha, \sin\theta_\alpha)$, where this angle θ_α performs rotational diffusion:

$$\partial_t \theta_\alpha = \sqrt{2D_r}\eta_\alpha(t) \tag{S48}$$

where $\eta_\alpha(t)$ is a Gaussian white noise with zero mean and correlation $\langle \eta_\alpha(t)\eta_{\alpha'}(t')\rangle = \delta(t-t')\delta_{\alpha\alpha'}$.

B. Mechanochemical Feedback

1. MCFL-I

The first mechanochemical feedback loop arises from the load-dependent binding of myosin to actin. When a cell is compressed, i.e., when the cell area A decreases, then the unbinding rate of myosin decreases which changes the preferred area A_0 and the preferred perimeter P_0 of the cell in the vertex model. In our model, the preferred area and perimeter undergo changes in an area-dependent manner. As mentioned in the main text, the actin reorganizes and concentrates along the cell-cell junctions as the tissue matures. This means that junctional tension should increase, and the contractility should decrease as a tissue matures. Such as effect must be accounted for by one positive and one negative MCFL. Since junctional tension is given by $-P_0/A_0^{3/2}$ and the contractility is given by A_0^{-1} [1], the feedback should be such that P_0 decreases with areal compression and A_0 should increase. Such a feedback can be accounted for in the following way:

$$\begin{aligned} \tau_A \partial_t A_0 &= -[A_0 - \hat{A}_0(A)] \\ \tau_P \partial_t P_0 &= -[P_0 - \hat{P}_0(A)] \end{aligned} \tag{S49}$$

where we see that the vertex model parameters A_0 and P_0 are time-dependent and they relax to area-dependent values $\hat{A}_0(A)$ and $\hat{P}_0(A)$. The $\hat{A}_0$ and $\hat{P}_0$ depend on the binding probability of myosin to actin. If the myosin-binding probability is given by $p_{bound} = 1/(1+(A/\hat{A})^2)$. Here, $\hat{A}$ is related to the dissociation constant K_d of myosin. Then, we know the constitutive relations from before:

$$\begin{aligned} \hat{A}_0 &= 2a_0 p_{bound} \\ \hat{P}_0 &= 2\hat{q}_0\sqrt{a_0}(1 - p_{bound}) \end{aligned} \tag{S50}$$

2. MCFL-II

To model the actin oscillations seen in experimental MDCK monolayers, we model ERK as a Hopf oscillator, which in this case is taken to be a Brusselator. Other Hopf oscillators also give similar collective behaviours as we have checked using the FItzhugh -Nagomo model [6]. The chemistry of the Hopf oscillator is coupled to the mechanics via areal compressions, just like in MCFL-I. The 1D version of the model has been studied before to model for ERK oscillations [6, 7]. The above Eq. S49 will now be modified as:

$$\begin{aligned}
\partial_t M &= a-(b+1)M+cM^2E \\
\partial_t E &= bM-cM^2E-DE \\
\tau_D\partial_t D &= -(D-D_0)-\beta D(A-1) \\
\tau_A\partial_t A_0 &= -[A_0-\hat{A}_0(A)]-\alpha(E-E_0) \\
\tau_P\partial_t P_0 &= -[P_0-\hat{P}_0(A)]-\frac{\alpha}{2\sqrt{A_0}}(E-E_0)
\end{aligned} \tag{S51}$$

where, E is ERK, M is MEK and D is a degrader of ERK, which couples the mechanics to the chemistry via the term $\beta D(A-1)$. The chemistry is coupled back to the mechanics via the terms $\alpha(E-E_0)$ and $\frac{\alpha}{2\sqrt{A_0}}(E-E_0)$.

3. Cell Divisions

To introduce cell divisions in our model, we will model each cell having a level of cyclin, c. The cyclin increases with time by the following growth law:

$$\frac{\partial c}{\partial t} = 1 \tag{S52}$$

A cell is picked with a probability rate r, and only if $c > c_{th}$ and $A > A_{th}$, where c_{th} is a threshold cyclin value and A_{th} is a threshold area, the picked cell is divided. The picked cell is divided by a line perpendicular to the long axis of the cell.

IV. ANALYSIS OF THE EXPERIMENTAL AND SIMULATION DATA

A. Ageing

To show ageing in simulation, we have calculated the overlap function $Q(t)$ and self-intermediate scattering function $F_s(k,t)$, for cell trajectories with different time origin t_{origin}. The $Q(t)$ plot is shown in Fig. T9 and the $F_s(k,t)$ plot is shown in Fig. T11.

To calculate the self-intermediate scattering function, we need to pick a wavevector, k. We use the k at which the static structure function $S(k)$ peaks [Fig. T10].

B. Force-moment tensor of a cell

Forces in the vertex model act on the vertices of a cell, c. If the position vector of vertex i is $\vec{r_i}$ and the force acting on it is $\vec{f_i}$, then the force moment tensor, Σ, is defined as:

$$\Sigma = \sum_{i\in V(c)} \vec{r_i}\otimes\vec{f_i} \tag{S53}$$

$$\therefore \Sigma_{mn} = \sum_{i\in V(c)} r_{i,m}f_{i,n}. \tag{S54}$$

Here, $V(c)$ is set of vertices belonging to the cell c, and m,n are the components of the vectors. The force-moment tensor serves as the analog of the stress tensor for a single cell. The trace (sum of the eigenvalues) of Σ measures

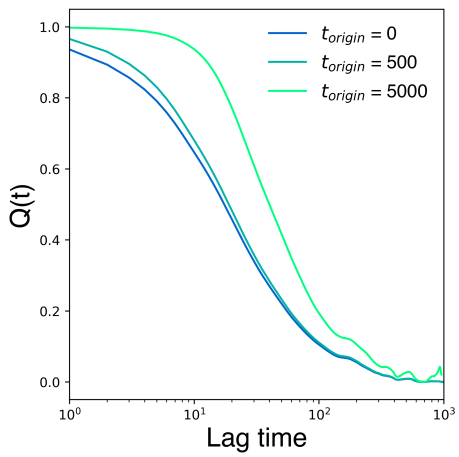

FIG. T9: $Q(t)$ for different t_{origin}, for $r = 100 \times 10^{-5}$ and $\hat{A} = 1.50$.

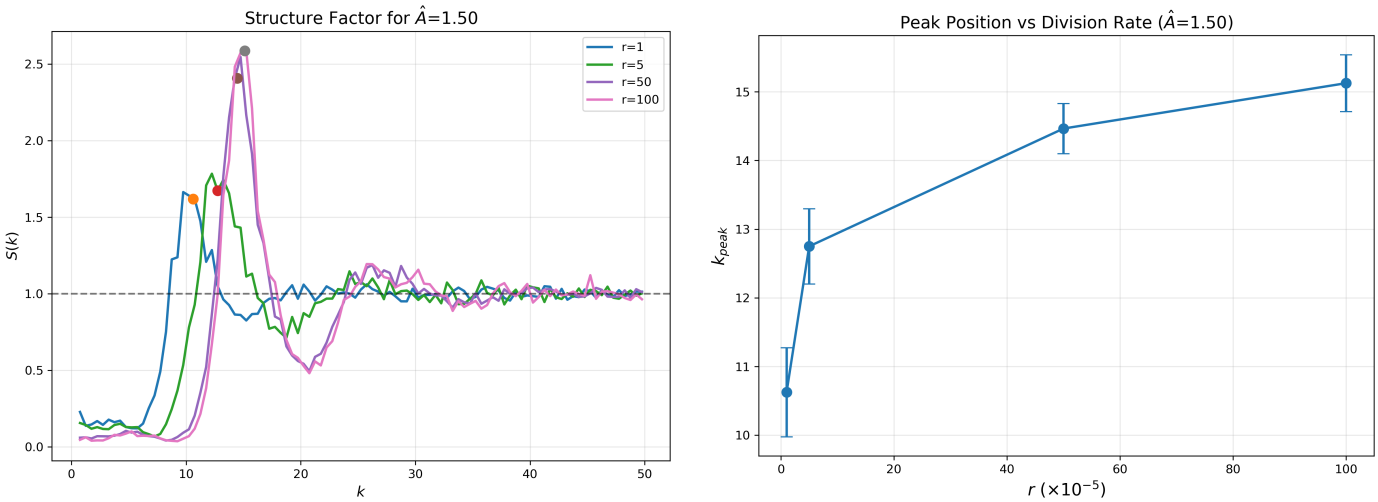

((a)) $S(k)$ for $r = 100 \times 10^{-5}$ and $\hat{A} = 1.50$.

((b)) k values corresponding to the peaks of $S(k)$.

FIG. T10: Structure factor from simulation.

the compressive stress at the cell, whereas the difference of the eigenvalues measure the shear stress. In thermal equilibrium, the standard deviation of $Tr.\Sigma$ is inversely proportional to the bulk viscosity and the standard deviation of the shear stress is inversely proportional to the shear viscosity. In out of equilibrium systems, such as the vertex model in this paper, the fluctuations and the viscosities are inversely related to each other, but the relationship does not arise from the conditions of thermal equilibrium.

C. Asphericity of cell shapes

We quantify the anisotropy of the cell shape using asphericity. To compute asphericity, we define the shape-moment tensor:

$$M = \sum_{i \in V(c)} \vec{r_i} \otimes \vec{r_i} \tag{S55}$$

$$\therefore M_{mn} = \sum_{i \in V(c)} r_{i,m} r_{i,n}. \tag{S56}$$

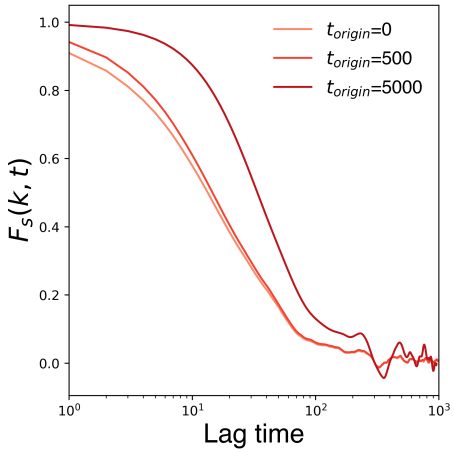

FIG. T11: $F_s(k,t)$ for different t_{origin}, for $k =$, $r = 100 \times 10^{-5}$ and $\hat{A} = 1.50$.

Next, we compute the eigenvalues of this matrix. In 2D, these are λ_1 and λ_2. The asphericity, κ, is defined as:

$$\kappa = \left| \frac{\lambda_1 - \lambda_2}{\lambda_1 + \lambda_2} \right|. \tag{S57}$$

For a nearly isotropic shape, such as a circle or a regular hexagon, $\kappa \to 0$, whereas for anisotropic shapes $\kappa > 0$ and approaches 1 for shapes with high aspect ratios. Geometrically, it is equivalent to fitting an ellipse to the underlying shape, whose semimajor and semiminor axis length are λ_1 and λ_2. We use this equivalence to calculate the asphericity of the MDCK cells in the experiments. Each segmented cell is fitted to an ellipse in trackmate, from which we compute the asphericities.

The asphericity here is related to the aspect ratio (AR) as follows:

$$\kappa = \left| \frac{\lambda_1 - \lambda_2}{\lambda_1 + \lambda_2} \right| = \left| \frac{\lambda_1/\lambda_2 - 1}{\lambda_1/\lambda_2 + 1} \right| = \left| \frac{AR - 1}{AR + 1} \right|. \tag{S58}$$

where the aspect ratio is given by $AR = \lambda_1/\lambda_2$. The asphericity κ is related to the aspect ratio, which has been shown to have a universal distribution for confluent epithelial monolayers [8].

D. Dynamic Heterogeneity Size Calculation

First we grid the system into a 25×25 boxes and average the velocities of cells in each box. This gives a velocity map of the system. After this, we find the grid points with the top 20% velocity. Following [9], we classify the dynamic heterogeneity region as the largest contiguous region (here, a collection of boxes) as the dynamic heterogeneity region and the size of that region as the dynamic heterogeneity size. Although [9] uses the top 10% velocity regions, this gave us a noisy result which is why we use the top 20% for our analysis.

E. Wavelet Analysis of the signal

We analyzed the spatiotemporal dynamics of both experimental and theoretical datasets using a unified framework. In the experimental system, actin-labeled images were acquired continuously over a 30-hour period with a temporal resolution of 30 minutes, yielding a sequence of spatially resolved intensity maps. In parallel, from simulations of our mechanochemical feedback model, we obtained the temporal evolution of the projected inverse area over the same time window. To make the two datasets directly comparable, the field of view in both cases was divided into a uniform 20×20 grid. Within each grid element, local time series data were extracted by averaging pixel intensities from actin images in the experiment, and inverse area images from the simulations.

A central consideration in this comparison is the correspondence between actin intensity in experiment and inverse area in simulation. Experimentally, actin accumulation reflects structural compaction: higher actin levels are

associated with smaller areas. Accordingly, we treated inverse area from simulations of our model as a proxy for actin concentration in the experimental data. This mapping enabled a consistent interpretation across modalities, thereby allowing theoretical predictions to be grounded in experimentally measurable quantities.

To isolate oscillatory components, the raw time series from both experiment and theory were first detrended using the PyBOAT software package. PyBOAT (A Biological Oscillations Analysis Toolkit) applies smoothing splines to remove low-frequency baseline trends, ensuring that slow variations in the signal do not mask the underlying oscillatory dynamics. After detrending, PyBOAT applies a continuous wavelet transform using the Morlet wavelet, generating a time–frequency representation of the signal. This approach captures transient and non-stationary oscillations that standard Fourier analysis would miss. From the resulting wavelet spectra, we extracted the dominant period and quantified the oscillation power for each grid element and then averaged the power values to obtain a representative measure of oscillatory strength, which was compared across simulated and experimental datasets. In the main text, to compare with the experiment, we choose $r = 50 \times 10^{-5}$, $c_{th} = 25$, and $\hat{A} = 1.50$ from our simulation in wavelet analysis.

V. CHOICE OF PARAMETERS

A. Choice of α and β

MCFL-II generates oscillations in the model, which has the mechanochemical couplings α and β. From simulations, we have found that the time period distributions of oscillations do not change with α and β but change with τ_D, τ_A and τ_P. We have chosen values $\alpha = 2.25$ and $\beta = 2.88$.

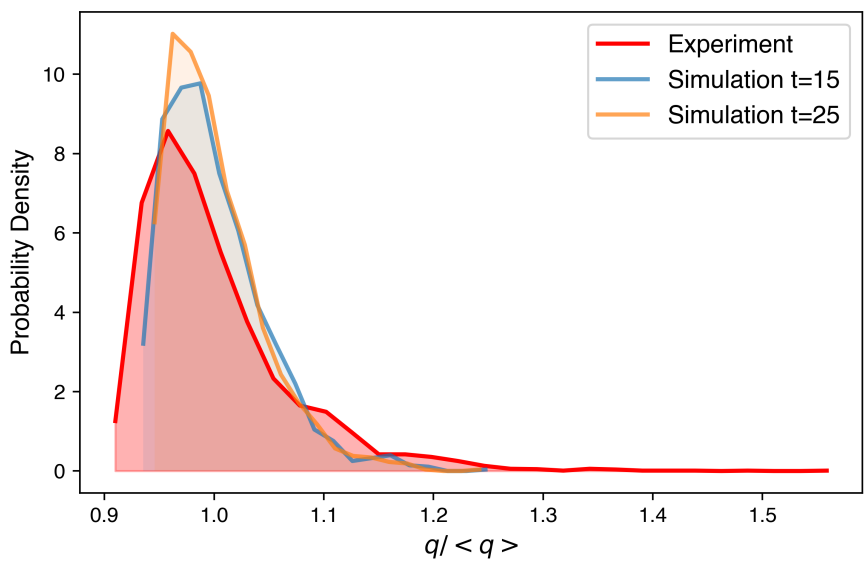

FIG. T12: Comparison of shape index distributions from experiment and simulation for $\alpha = 2.25$ and $\beta = 2.88$.

B. Choice of τ_D, τ_A, τ_P

The time period of oscillations generated by MCFL-II depends on τ_D, τ_A and τ_P. We have chosen the values by comparing the distributions with the experimentally observed distributions.

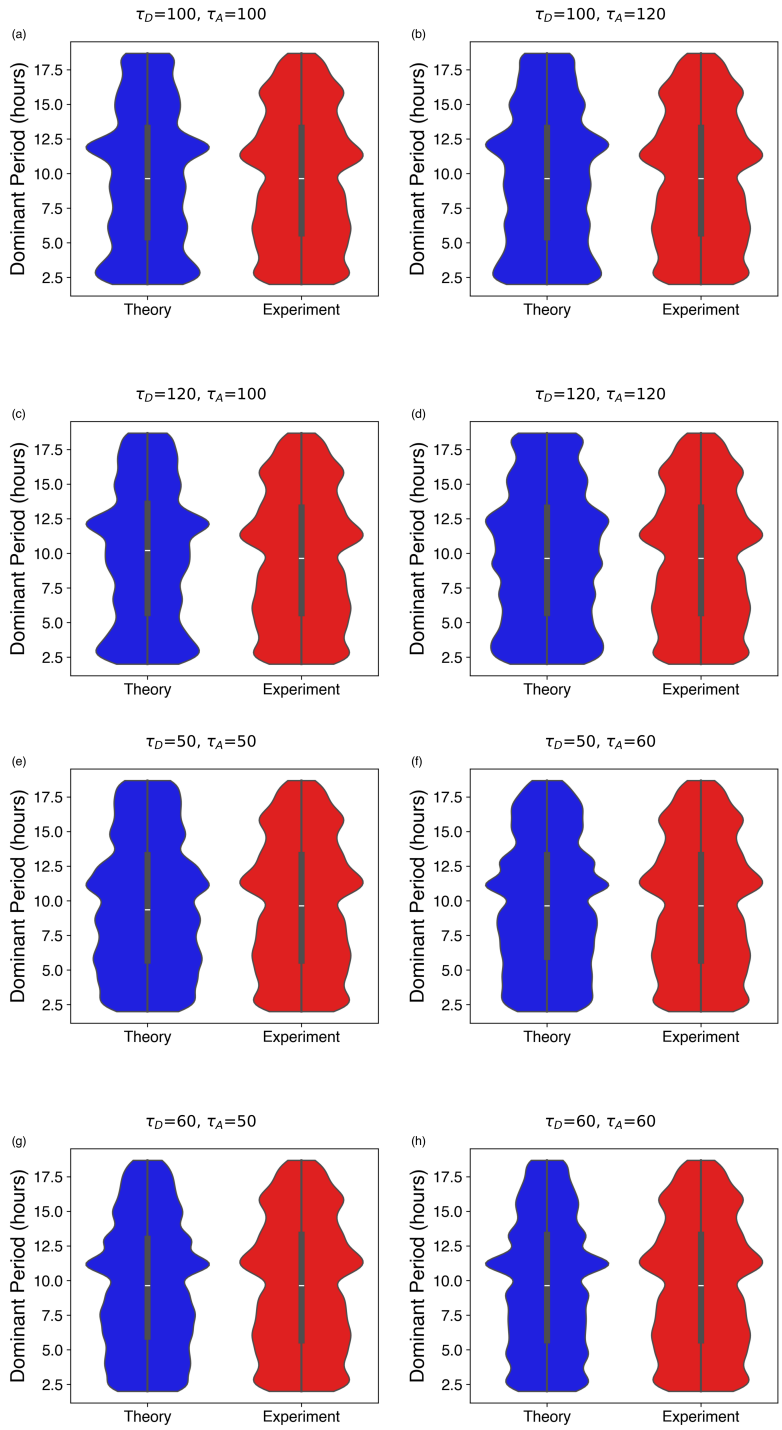

FIG. T13: Violin plots showing the dominant time period distributions compared with the same obtained from experimental data. Here, $\tau_A = \tau_P$, $\hat{A} = 1.50$, $r = 50 \times 10^{-5}$.

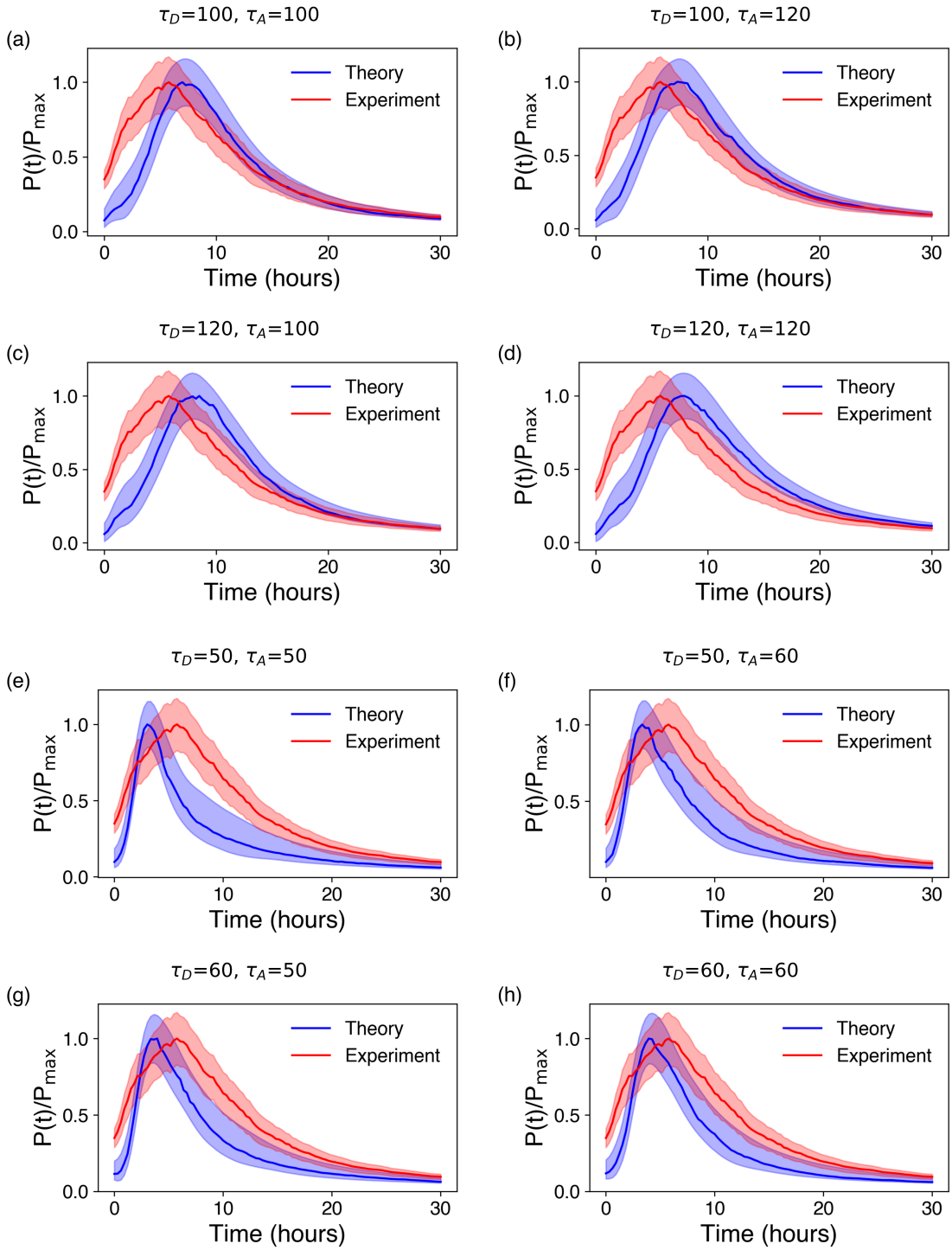

FIG. T14: Power time series plots comparison between experiment and simulation. Here, $\tau_A = \tau_P$, $\hat{A} = 1.50$, $r = 50 \times 10^{-5}$.

By observing that the distributions match best for $\tau_D = \tau_A = \tau_P = 120$, we use those values for the simulations.

C. Choice of r, c_{th} and A_{th}

We have chosen the values of r and c_{th} by comparing the simulation data with the experimentally observed growth rate.

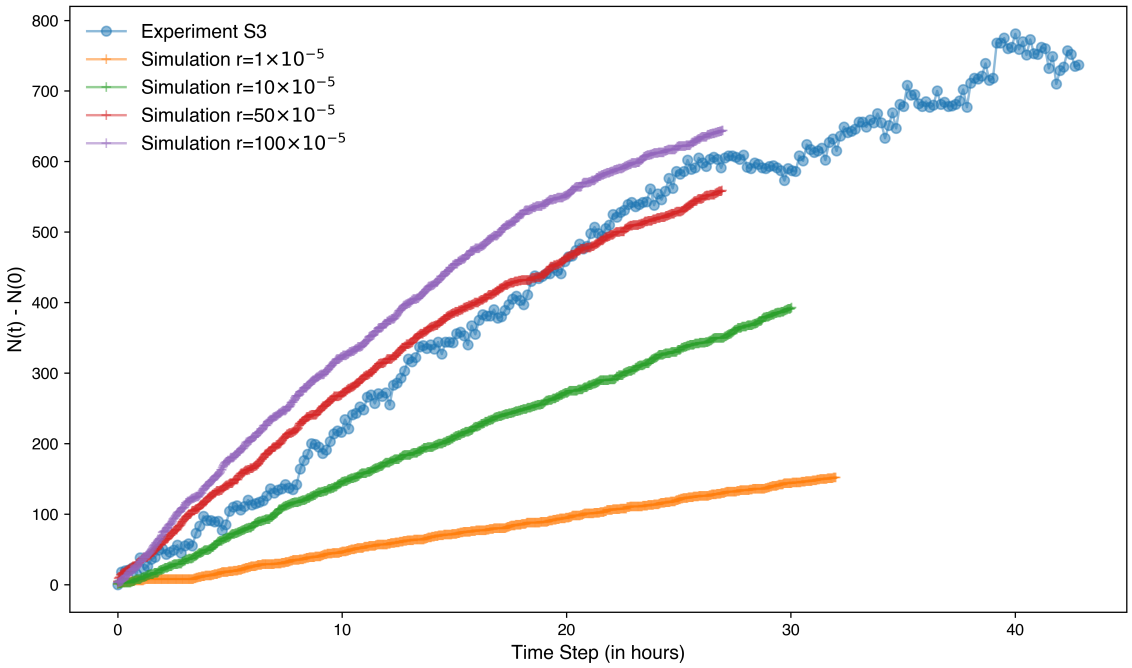

FIG. T15: Cell number growth for different division rates, r, for $c_{th} = 25$.

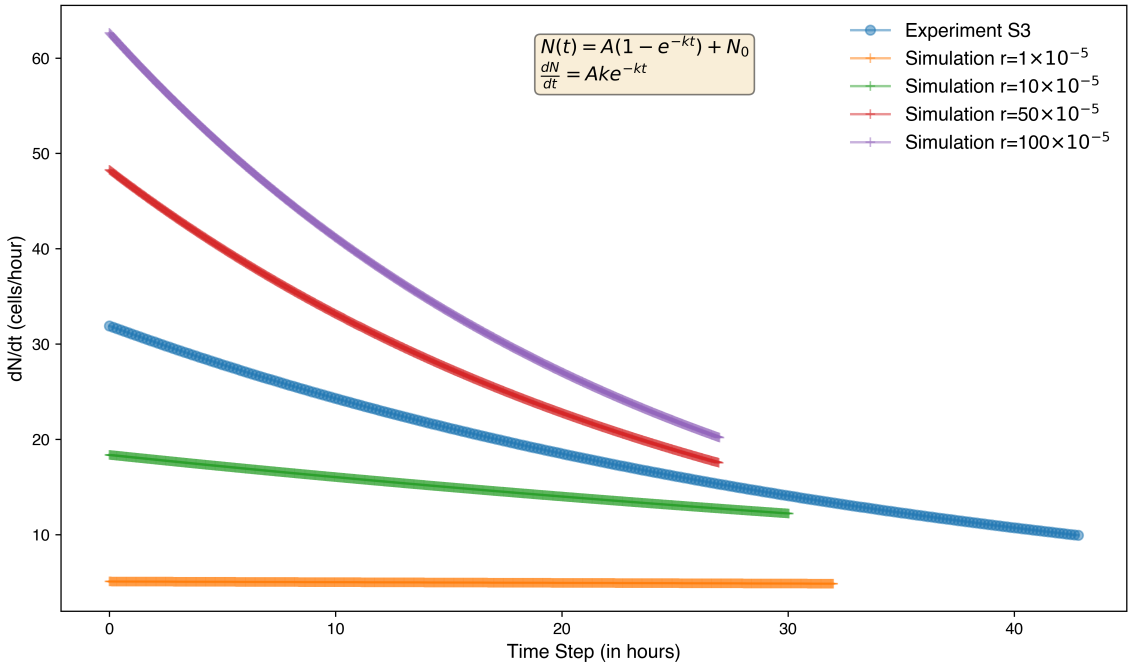

FIG. T16: Cell number growth rate for different division rates, r, for $c_{th} = 25$.

The $N(t)$ curve for simulations plateaus as the areas of the cells continuously decrease with time in the simulation,

which is visible from the decrease of dN/dt decreasing with time. We have obtained $\frac{dN}{dt}(t)$ by fitting a function $N(t) = A(1 - e^{-kt}) + N_0$ to the $N(t)$ data and then finding $\frac{dN}{dt} = Ake^{-kt}$. The time at which the $N(t)$ starts to plateau depends on the value of A_{th}. The value in simulations is taken as $A_{th} = 0.3$.

Moreover, we see that the time period distribution matches better for the r ($\approx 10^{-4}$) values, which match the experimental growth rate.

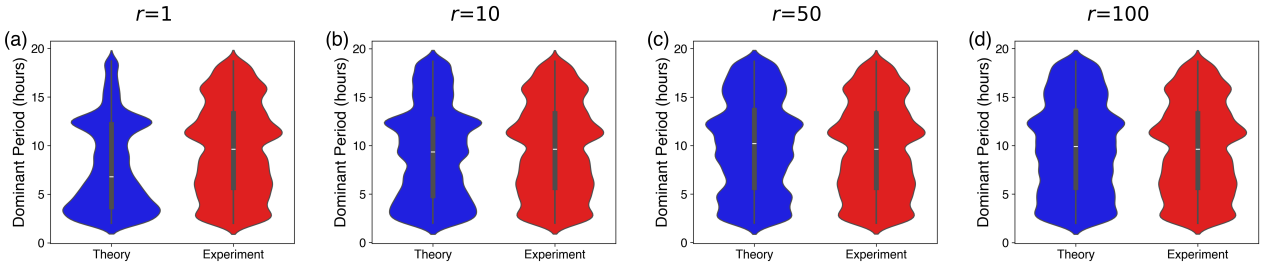

FIG. T17: Comparison between the dominant time period distributions from simulation and experiment for different r (in $\times 10^{-5}$) and $c_{th} = 25$.

The growth rate dN/dt in simulations varies with the parameters r and c_{th} as given below:

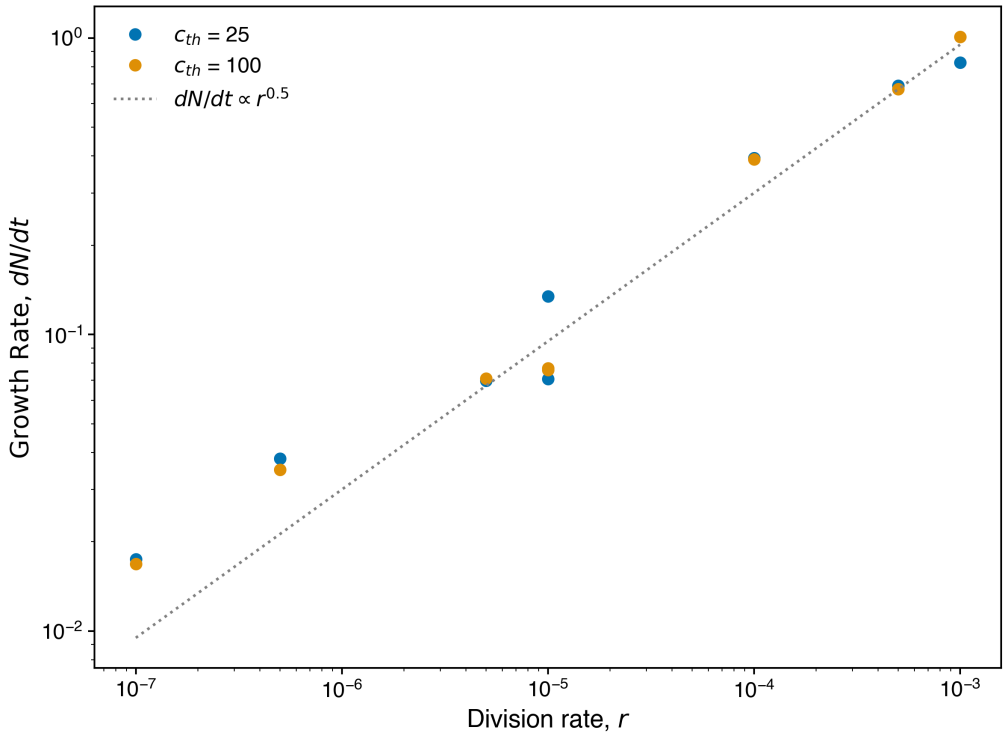

FIG. T18: Growth rates for different r and c_{th}.

The growth rate here is calculated by fitting a straight line to the initial increase in the $N(t)$ data from simulations.

D. Parameters Used

Parameter	Value
K	1.2 [5]
Γ	0.38 [5]
ζ	1
$\hat{q}_0$	3.9
v_0	0.125
D_r	0.5
$\tau_D = \tau_A = \tau_P$	120
Δt	0.01

- **Simulation and Experimental timescales:** 1 simulation time step = 2 minutes in experiment.
- The values of other parameters is mentioned in the main text figures.
- **Topological transitions:** The simulation has the following topological transitions:
  - T1 transitions
  - T2 transitions: cell divisions
  - A node switch operation have also been implemented to prevent overlaps [10].

REFERENCES

1. Farhadifar, R., Röper, J.-C., Aigouy, B., Eaton, S. & Jülicher, F. The Influence of Cell Mechanics, Cell-Cell Interactions, and Proliferation on Epithelial Packing. *Current Biology* **17,** 2095–2104. ISSN: 0960-9822. http://dx.doi.org/10.1016/j.cub.2007.11.049 (Dec. 2007).
2. Staple, D. B. *et al.* Mechanics and remodelling of cell packings in epithelia. *The European Physical Journal E* **33,** 117–127. ISSN: 1292-895X. http://dx.doi.org/10.1140/epje/i2010-10677-0 (Oct. 2010).
3. Abhishek, M., Dhanuka, A., Banerjee, D. S. & Rao, M. Excitability and travelling waves in renewable active matter. *arXiv preprint arXiv:2503.19687* (2025).
4. Sknepnek, R., Djafer-Cherif, I., Chuai, M., Weijer, C. & Henkes, S. Generating active T1 transitions through mechanochemical feedback. *Elife* **12,** e79862 (2023).
5. Boocock, D., Hirashima, T. & Hannezo, E. Interplay between mechanochemical patterning and glassy dynamics in cellular monolayers. *PRX Life* **1,** 013001 (2023).
6. Dewan, P., Mondal, S. & Sarkar, S. *Oscillation death by mechanochemical feedback* 2025. arXiv: 2504.19655 [cond-mat.soft]. https://arxiv.org/abs/2504.19655.
7. Boocock, D., Hino, N., Ruzickova, N., Hirashima, T. & Hannezo, E. Theory of mechanochemical patterning and optimal migration in cell monolayers. *Nature Physics* **17,** 267–274. ISSN: 1745-2481. http://dx.doi.org/10.1038/s41567-020-01037-7 (Sept. 2020).
8. Sadhukhan, S. & Nandi, S. K. On the origin of universal cell shape variability in confluent epithelial monolayers. *eLife* **11** (eds Kruse, K., Walczak, A. M. & Joanny, J.-F.) e76406. ISSN: 2050-084X. https://doi.org/10.7554/eLife.76406 (Dec. 2022).
9. Angelini, T. E. *et al.* Glass-like dynamics of collective cell migration. *Proceedings of the National Academy of Sciences* **108,** 4714–4719. eprint: https://www.pnas.org/doi/pdf/10.1073/pnas.1010059108. https://www.pnas.org/doi/abs/10.1073/pnas.1010059108 (2011).
10. Fletcher, A. G., Osborne, J. M., Maini, P. K. & Gavaghan, D. J. Implementing vertex dynamics models of cell populations in biology within a consistent computational framework. *Progress in Biophysics and Molecular Biology* **113,** 299–326. ISSN: 0079-6107. https://www.sciencedirect.com/science/article/pii/S0079610713000989 (2013).